



**US Army Corps  
of Engineers<sup>®</sup>**  
Engineer Research and  
Development Center

**ERDC**  
INNOVATIVE SOLUTIONS  
for a safer, better world

*Materials Modeling for Force Protection*

## **Comparison/Validation Study of Lattice Boltzmann and Navier-Stokes for Various Benchmark Applications**

Report 1 in “Discrete Nano-Scale Mechanics and Simulations” Series

Jeffrey B. Allen, Wayne D. Hodo, Laura Walizer,  
David P. McInnis, Alex Carrillo, Bohumir Jelinek,  
Daniel Johnson, John Peters, and Sergio D. Felicelli

September 2014

**The U.S. Army Engineer Research and Development Center (ERDC)** solves the nation's toughest engineering and environmental challenges. ERDC develops innovative solutions in civil and military engineering, geospatial sciences, water resources, and environmental sciences for the Army, the Department of Defense, civilian agencies, and our nation's public good. Find out more at [www.erdc.usace.army.mil](http://www.erdc.usace.army.mil).

To search for other technical reports published by ERDC, visit the ERDC online library at <http://acwc.sdp.sirsi.net/client/default>.

# **Comparison/Validation Study of Lattice Boltzmann and Navier-Stokes for Various Benchmark Applications**

Report 1 in "Discrete Nano-Scale Mechanics and Simulations" Series

Jeffrey B. Allen

*Information Technology Laboratory  
U.S. Army Engineer Research and Development Center  
3909 Halls Ferry Road  
Vicksburg, MS 39180-6199*

Wayne D. Hodo, Laura E. Walizer, and David P. McInnis

*Geotechnical and Structures Laboratory  
U.S. Army Engineer Research and Development Center  
3909 Halls Ferry Road  
Vicksburg, MS 39180-6199*

Alex Carrillo

*Coastal and Hydraulics Laboratory  
U.S. Army Engineer Research and Development Center  
3909 Halls Ferry Road  
Vicksburg, MS 39180-6199*

Bohumir Jelinek, Daniel Johnson, and John Peters

*Center for Advanced Vehicular Systems  
Mississippi State University  
Mississippi State, MS 39762*

Sergio D. Felicelli

*Mechanical Engineering Department, University of Akron  
302 E. Buchtel Avenue  
Akron, OH 44325*

Final report

Approved for public release; distribution is unlimited.

Prepared for U.S. Army Corps of Engineers  
Washington, DC 20314-1000

Under AT22/AT40 program, "Materials Modeling for Force Protection;" Work Units  
#PM001 and #MR001: "Discrete Nano-Scale Mechanics and Simulations."

## Abstract

For purposes relating to the U.S. Army's need for materials modeling and force protection, this work provides justification for assigning effective equivalence between two commonly used fluid simulation methods—namely the Navier-Stokes (NS) and Lattice Boltzmann methods. The Lattice Boltzmann Method (LBM) has become increasingly popular as an alternative approach to traditional NS-based techniques for modeling various incompressible fluid flow applications. The LBM has recently increased its range of applicability to include numerous fields of interest including those involving multiphase and thermo-fluid structure interactions. This report documents a comparison/validation effort accompanying the development of a standard Lattice Boltzmann solver with immersible moving boundaries. The primary goal is to validate the model by comparing it with various laminar, incompressible flow cases simulated using a finite volume-based NS solver. Simulations involving four standard benchmark studies were analyzed: (1) the flow through a rectangular channel, (2) the flow through a lid-driven cavity, (3) the flow over a back-step, and (4) the flow over a stationary circular cylinder. For the specific applications and Reynolds numbers simulated, the results showed excellent agreement between the two cases. Disparities were observed only when the theoretical constraints of the LBM were exceeded.

**DISCLAIMER:** The contents of this report are not to be used for advertising, publication, or promotional purposes. Citation of trade names does not constitute an official endorsement or approval of the use of such commercial products. All product names and trademarks cited are the property of their respective owners. The findings of this report are not to be construed as an official Department of the Army position unless so designated by other authorized documents.

**DESTROY THIS REPORT WHEN NO LONGER NEEDED. DO NOT RETURN IT TO THE ORIGINATOR.**

# Contents

<b>Abstract.....</b>	<b>ii</b>
<b>Contents.....</b>	<b>iii</b>
<b>Figures and Tables.....</b>	<b>iv</b>
<b>Preface .....</b>	<b>vi</b>
<b>Notation .....</b>	<b>vii</b>
<b>1 Introduction .....</b>	<b>1</b>
1.1 Background.....	1
1.2 Objective.....	5
1.3 Approach .....	5
<b>2 Navier-Stokes Equations .....</b>	<b>7</b>
2.1 Isothermal and incompressible flows.....	8
2.2 Finite volume discretization .....	8
<b>3 Lattice Boltzmann Equation .....</b>	<b>11</b>
<b>4 Lattice Boltzmann/Navier-Stokes Equivalence using the Chapman-Enskog Expansion.....</b>	<b>15</b>
<b>5 Implementation Issues.....</b>	<b>20</b>
<b>6 Lattice Boltzmann and Navier-Stokes Benchmark Applications.....</b>	<b>22</b>
6.1 Rectangular channel flow.....	24
6.1.1 <i>Problem description and setup</i> .....	24
6.1.2 <i>Results</i> .....	24
6.2 Flow through a lid-driven cavity.....	28
6.2.1 <i>Problem description and setup</i> .....	28
6.2.2 <i>Results</i> .....	28
6.3 Rectangular channel flow with back-step .....	31
6.3.1 <i>Problem description and setup</i> .....	31
6.3.2 <i>Results</i> .....	36
6.4 Flow over a stationary circular cylinder .....	37
6.4.1 <i>Problem description and setup</i> .....	37
6.4.2 <i>Results</i> .....	39
<b>7 Summary and Conclusions .....</b>	<b>44</b>
<b>References.....</b>	<b>45</b>
<b>Appendix A: Derivation of the Equilibrium Distribution Function .....</b>	<b>49</b>

# Figures and Tables

## Figures

Figure 1. One-dimensional control volume used in the FVM.....	9
Figure 2. Position and velocity vectors resulting from an external force.....	11
Figure 3. Lattice velocities corresponding to the D2Q9 configuration.....	13
Figure 4. Velocity profiles comparing the results of the LBM and NS corresponding to the flow through a rectangular channel (a) $Re = 200$ , (b) $Re =$ 400, and (c) $Re = 800$ ). A velocity inlet condition is used. As indicated, the velocities were sampled at three downstream locations corresponding to $X/L =$ 0.1, $X/L = 0.2$ and $X/L = 0.5$ . (Lattice/grid resolution = 1000x40). .....	25
Figure 5. Velocity profiles comparing the results of the LBM and NS corresponding to the flow through a rectangular channel ( $Re = 200$ , $Re = 400$ , and $Re = 800$ ). A pressure gradient condition is used. As indicated, the velocities were sampled at three downstream locations corresponding to $X/L = 0.1$ , $X/L =$ $0.2$ and $X/L = 0.5$ . (Lattice/grid resolution = 1,000x40).....	27
Figure 6. Representative velocity convergence error per Eq. 61 for the flow through a rectangular channel. As shown, approximately 2,000 LBM iterations were required for fully steady-state conditions.....	27
Figure 7. Velocity contours comparing the results of the LBM and Navier-Stokes for flow through a lid-driven cavity ( $Re = 100$ , $Re = 1,000$ and $Re = 3,000$ ). As shown, the presence of a large central vortex is observed for each case, as well as several secondary vortices (lattice/grid resolution:100x100). .....	29
Figure 8. Velocity profiles comparing the results of the LBM and NS for flow through a lid-driven cavity ( $Re = 100$ , $Re = 1,000$ and $Re = 3,000$ ). As indicated, the x-component and y-component of velocity were sampled along the vertical and horizontal domain centerlines, respectively.....	31
Figure 9. Geometry corresponding to the flow over a back-step.....	32
Figure 10. Velocity contours for $Re = 200$ (a), $Re = 400$ (b), $Re = 800$ (c), and $Re=1000$ (d) were conducted using the LBM. The contours show a large vortex aft of the back-step (as well as a secondary circulation zone for $Re = 1,000$ ) that increases in size with increasing Reynolds number (lattice/grid resolution:100x100).....	33
Figure 11. Velocity profiles comparing the results of the LBM and NS corresponding to the flow over a back-step ( $Re = 200$ (a), $Re = 400$ (b) and $Re =$ 800 (c)). As indicated, the velocities were sampled at three downstream locations corresponding to $X/L = 0.1$ , $X/L = 0.2$ and $X/L = 0.5$ (lattice/grid resolution = 1,000x40).....	34
Figure 12. Reattachment distance as a function of Reynolds number. Results using the LBM are compared with the experiments conducted by Le and Moin (1994). .....	35
Figure 13. Illustration of velocity profiles as a function of Reynolds number ( <a href="http://en.wikipedia.org/wiki/Reynolds_number">http://en.wikipedia.org/wiki/Reynolds_number</a> ). .....	38

---

Figure 14. Geometry corresponding to the flow over a stationary circular cylinder. ....	38
Figure 15. Velocity contours for $Re = 1$ , $Re = 10$ , and $Re = 120$ show results from both the LBM and NS method. The contours reveal the characteristic steady to unsteady flow behaviors associated with increasing Reynolds number, and show the presence of Von Karman vortex shedding for $Re = 120$ . (Lattice/grid resolution: 2000x400.).....	40
Figure 16. Velocity profiles comparing the results of the LB and NS methods corresponding to the flow over a stationary circular cylinder ( $Re = 1$ , and $Re = 10$ ). As indicated, the velocities were sampled at three downstream locations corresponding to $X/L = 0.1$ , $X/L = 0.2$ and $X/L = 0.5$ . (Note: lattice/grid resolution = 2,000x400). .....	42
Figure 17. Time history of the drag coefficient computed using Eq. 66. The results shown are from the LBM for $Re=120$ .....	43

## Tables

Table 1. Simulation parameters used for the rectangular channel flow problem. ....	24
Table 2. Simulation parameters used for lid-driven cavity problem.....	28
Table 3. Simulation parameters used for the back-step channel flow problem. ....	32
Table 4. Simulation parameters used for the back-step channel flow problem. ....	39

## Preface

This study was conducted for the U.S. Army Corps of Engineers under AT22/AT40 program, “Materials Modeling for Force Protection,” Work Units PM001 and MR001, “Discrete Nano-Scale Mechanics and Simulations.”

The research and development effort was led by the Airfields and Pavements Branch (CEERD-GM-A) of the US Army Engineer Research and Development Center—Geotechnical and Structures Laboratory (ERDC-GSL). This report was prepared under the general purview of Dr. David Horner (CEERD-GZT), Technical Director of the Military Engineering Research Program, and under the general direction of three ERDC laboratory directors: Dr. Reed Mosher (ITL; CEERD-IZA), Dr. David Pittman (GSL; CEERD-GZA), and Mr. Jose E. Sanchez (CHL; CEERD-HZ).

Assisting with the solver development and the report’s technical content, collaborations with Mississippi State University’s Center for Advanced Vehicular Systems (CAVS) were of significant benefit, with Dr. Sergio Felicelli serving as supervisor (now serving as Professor and Chair of the Mechanical Engineering Department at the University of Akron).

COL Jeffrey R. Eckstein was the Commander of ERDC, the Associate Director of ERDC was Dr. John Cullinane, and the ERDC Executive Director was Dr. Jeffery P. Holland.

# Notation

## Acronyms/Symbols

- $AR$ : aspect ratio
- BGK: Bhatnagar-Gross-Krook
- CAVS: Center for Advanced Vehicular Systems
- CFD: computational fluid dynamics
- DEM: discrete element method
- FDM: finite difference method
- FEM: finite element method
- FVM: finite volume method
- IMB: immersible moving boundary
- $Kn$ : Knudsen number
- LBM: Lattice Boltzmann method
- $Ma$ : Mach number
- MRT: multiple relaxation time
- NS: Navier-Stokes method
- PISO: pressure implicit with splitting operator
- $Re$ : Reynolds number

## Notation

- $f^{eq}$ : equilibrium distribution function
- $\rho$ : fluid density
- $c_s$ : speed of sound
- $\vec{u}$ : fluid velocity
- $\vec{c}$ : lattice velocity
- $p$ : pressure
- $T$ : temperature
- $E$ : energy (internal)
- $t$ : time
- $\vec{x}$ : position coordinate
- $\kappa$ : thermal conductivity
- $I$ : identity matrix
- $S$ : strain rate tensor
- $\tau$ : deviatoric stress tensor
- $\mu'$ : bulk viscosity

- $\nu$ : kinematic viscosity
- $\mu$ : dynamic (shear) viscosity
- $R$ : gas constant
- $w_i$ : lattice weights
- $l$ : mean free path
- $\epsilon$ : Knudsen number ( $Kn = l/L$ )
- $\vec{\omega}$ : angular velocity
- $\varepsilon$ : volume fraction of a lattice cell (used in IMB approach)
- $B_n$ : weighting function (used in IMB approach)
- $\tau$ : relaxation time
- $\omega$ : relaxation frequency ( $1/\tau$ )
- $\Omega_i^S$ : collision operator (used in IMB approach)
- $\Omega_i^{BGK}$ : Bhatnagar-Gross-Krook (BGK) collision operator
- $L$ : domain length
- $H$ : domain height
- $A$ : area
- $\delta$ : Kronecker function ( $\delta_{ij} = 1$  if  $i = j$ , else  $\delta_{ij} = 0$ )
- $N$ : number of lattice sites ( $\hat{L}/\hat{\delta}_x$ )
- $\delta_x$ : spatial discretization step
- $\delta_t$ : temporal discretization step
- $\vec{F}$ : external force
- $\vec{g}$ : acceleration due to gravity
- $C_v$ : Specific heat at constant volume
- $C_d$ : Coefficient of drag

## Operations

- $\vec{\nabla}$ : gradient operator
- $\vec{a} \cdot \vec{b}$ : scalar product ( $\vec{a} \cdot \vec{b} = \sum_i a_i b_i$ )
- $\nabla^2$ : Laplace operator
- $\langle \quad \rangle$ : Average operation

## Subscripts

- $\alpha, \beta, \gamma$ : coordinate indices
- cm: center of mass
- $i$ : lattice cell index
- p: reference point
- $e, w, n, s$ : directional indices (used in Finite Volume discretization)

## Superscripts

- $\hat{\cdot}$ : related to lattice quantities (i.e.,  $\hat{\delta}_x$  is the lattice spatial discretization step)

(This page intentionally left blank.)

# 1 Introduction

## 1.1 Background

The Lattice Boltzmann method (LBM) is becoming increasingly popular as an alternative approach to traditional techniques for modeling various fluid flow applications. More traditional approaches such as the Navier-Stokes (NS)-based finite difference method (FDM), the finite element method (FEM), or the finite volume method (FVM) are founded on the discretization of macroscopic equations at the continuum level. By contrast, the LBM is based on distribution functions describing the kinetic behavior of particles that are characteristic of microscale and mesoscale simulations (Griebel; et al. 1997; Al-Jahmany 2004; Zienkiewicz et al. 2005; Canuto et al. 1988).

The use of the LBM approach for numerically simulating secondary (amorphous) phase constituents (most often represented as a laminar, incompressible fluid) within the context of material science-based applications is, for our purposes, strategically based on two primary motivations. The first of these motivations, and possibly the most dominant, relates to the omnipresent problem of spatiotemporal scale compatibility and reconciliation, wherein one attempts to make macroscale material decisions based on microscale or nanoscale performance criteria. The second motivation relates to concerns over mesh quality and the ability of the method being used to accurately resolve the flow over complex shapes.

With respect to scale compatibility, the LBM is derived from a strictly atomistic (though probabilistic) parent method. Known as the Boltzmann equation, the parent method describes the phenomenological properties of microscale, particulate systems via the use of a phase space distribution function. Particularly attractive, is the fact that the method allows for the direct computation of macroscopic variables (e.g., velocity, density, pressure) through a system of moment-based equations, as well as information at the microscale, vis-à-vis direct interpretation of the distribution function. The LBM derivation parallels its parent method in every particular, except that it allows for a more simplified estimation of the probability distribution function via a set of discrete velocities situated on a structured lattice framework. Multiscale applicability is thus also an inherent feature within this method, as it has successfully demonstrated its capacity to

solve a number of problems at both the micro and continuum scales (Raabe 2004; Succi et al. 1993). The more traditional methods (e.g., Euler, NS, Burnett), though arguably more ubiquitous in their usage (owing to their extended level of maturity, and familiarity), are nevertheless derived strictly from a continuum-based assumption. Apart from a few exceptions (e.g., the use of slip wall boundary conditions to extend the NS method into regimes of larger Knudsen number [ $Kn$ ]), these methods are quite limited for purposes of spatiotemporal scaling.

The second argument in support of using the LBM approach concerns the issue of accurately resolving the flow field dynamics surrounding complex shapes. Grain structures (static, dynamic, isotropic, anisotropic), structural asperities, irregular flow channels, inclusions, etc. are common features found in many material science applications. Most traditional methods rely on highly resolved (unstructured) grid approaches to model these complex geometries. Unfortunately, these traditional methods are subject to several potential drawbacks, including:

- Computational costs due to the large volume of elements required to adequately resolve “small tight spaces” and areas of large flow gradients.
- Concerns over mesh quality, which inevitably occur in conjunction with the computation cost drawback just above and include such items as negative element volumes, highly skewed elements, and improper surface normal assignments.
- Time and resource costs due to the excessive labor requirements to implement quality grid(s). (This often-underestimated concern consumes the vast majority of a researchers’ time and resources, often resulting in the separate hire of a “meshing expert”).

The LBM approach is effectively immune from these drawbacks due in large part to the development of the immersible moving boundary (IMB) method (Owen et al. 2011). While the LBM does utilize a simple structured regular lattice, the IMB method operates in a manner that is completely independent and distinct from the underlying mesh density. The IMB method is based on the adaptation of the LBM collision operator which accounts for the limited area or volume fraction of a lattice cell, subject to an intruding surface or volume. While it is still necessary to provide a reliable method for the computation of the said area or volume fraction (de-

pending on the prescribed level of accuracy), there are typically a variety of proven methods that are readily practicable.

Additional advantages of the LBM over the more conventional approaches include the following:

- The LBM is relatively simple to implement. Unlike other solvers, LBM models flow fields explicitly. Each time step can be split into a streaming step and a collision step involving no matrix inversion processes. The development of the standard Bhatnagar-Gross-Krook (BGK) collision operator (Higuera and Jimenez 1989; Koelman 1991) further eases implementation by providing a dramatically simplified alternative to the cumbersome integrodifferential collision operator of the standard Boltzmann equation.
- The LBM provides excellent scalability for large, parallel applications. All interactions in the LBM are strictly local. In the collision step, the updated distribution function at a given lattice site is computed by involving only the information at the same node. In the propagation step, each lattice site must exchange information only with its nearest-neighbor lattice sites.
- The convection term in the LBM is linear. In contrast to the second-order non-linear convection term in the NS equations, the linearity of the LBM convection term results in significant time savings. The LBM recovers the same second-order accuracy as the NS equations through a relaxation process involving particle interactions.
- Unlike NS-based solutions, an explicit solution for the pressure dynamics is not required in the LBM approach. The pressure in the LBM is computed from the ideal gas law. The NS approach involves a separate iterative solution involving the Poisson equation. This calculation is one of the most time-consuming operations of the NS method.

As a consequence of these recent advances, the LBM has extended its range of applicability to include:

- simulations of turbulent flows (Eggels 1996),
- suspension of colloidal particles (Ladd 2001),
- porous media (Gunstensen et al. 1991),
- multiphase and multicomponent flows (Grunau et al 1993; Shan and Chen 1993), and
- magnetohydrodynamics (Chen et al. 1991).

Other LBM-based research efforts that have been specifically conducted at ERDC include:

- simulation of viscous flow through a column of glass beads (Maier et al. 1998),
- investigations involving the effects of pore geometry on transport mechanisms to better characterize constitutive relationships in multi-phase flows (Maier et al. 1996), and
- simulations involving the accuracy of the LBM as relating to Mach number, spatial resolution, boundary conditions and the lattice mean free path (Maier and Bernard 1997).

Additionally, or in many cases complementary to the aforementioned listing, the LBM has recently been developed for thermofluid structure interaction applications via hydrodynamic and/or thermal coupling mechanisms. This latest development has, for example, facilitated the use of coupled discrete element method (DEM)/LBM models that can be used in a large variety of applications of interest, including those relating to: porous media flows (Han and Cundall 1997) (including fines migration applications), geologic deformation (shear) band permeability evolution (Sun et al. 2013), gas-fluidized beds (Third and Müller 2013), and liquid phase sintering (Varnick et al. 2013).

Despite the increased progress and stated advantages of the LBM over conventional approaches, the total number of publications resulting from LBM research is substantially in the minority, compared to more conventional approaches. This paucity in LBM research is likely due to its relative novelty, but it may also be attributable to various difficulties relating to implementation issues, including: the indirect method of applying boundary conditions (i.e., prescribing distribution functions in lieu of explicitly providing Dirichlet or Neumann conditions involving precise macroscopic variables), the need to prescribe aspect ratio and Reynolds number ( $Re$ ) equivalence when making model comparisons, the use of lattice units as compared with physical ( $Re$ ) units, or the numerical instabilities that can arise for violations of compressibility or laminar restraints. Additional liabilities of the LBM include (Mohamad 2011):

- The difficulty in simulating high Mach number ( $Ma$ ) flows (in excess of the incompressible limit – e.g.,  $Ma > 0.3$ ).

- Local violations of the  $Kn$ . which are particularly likely for flows with strong velocity gradients.
- The limitations associated with uniform square grids. As opposed to conventional FVM, FEM, or FDM approaches, the LBM is primarily restricted to square lattices. Refinement meshing and/or the application of curved grids have proven difficult to implement.
- The LBM is subject to numerical instabilities particularly when the lattice viscosity ( $\hat{\nu}$ ) becomes too small.

## 1.2 Objective

While there is currently no debate concerning the theoretical equivalence of the LBM and NS for low  $Ma$  flows with negligible density fluctuation (the Chapman-Enskog expansion conclusively proves this, as discussed in Chapter 4); in practice however, negligible density fluctuations can be difficult to achieve. This difficulty is particularly true for imposed pressure boundary conditions. In fact, regardless of the imposed boundary conditions, the spatial density variation is never completely zero in LBM simulations. Other potential problems underlying the traditional LBM are associated with local stability issues, particularly those brought on by local flow gradients.

In light of the aforementioned concerns, this report documents a comparison/validation effort accompanying the development of a standard LBM solver complemented with the IMB method. For validation purposes, conventional NS methods are utilized. In particular, comparison studies will involve four standard benchmark cases including, the flow through a rectangular channel, the flow inside a lid driven cavity, the flow over a back-step, and the flow over a stationary circular cylinder. Each case will be simulated over a variety of different input conditions and associated Reynolds numbers.

## 1.3 Approach

This report first presents the incompressible, laminar, NS equations (including the continuity equation). The need to include the Poisson equation is demonstrated for purposes of closure. For illustration purposes, a simple one-dimensional convection-diffusion example is presented and discretized in accordance with the FVM of solution. Second, the theoretical background for the LBM is presented with origins derived from the standard Boltzmann equation. In lieu of the complex

integrodifferential collision operator of the standard Boltzmann equation, the standard BGK approximation is used (Higuera and Jimenz 1989; Koelman 1991). Third, assuming negligible density variation, the analytical equivalence between the LBM and NS is shown using the Chapman-Enskog expansion method. Finally, the aforementioned benchmark comparison studies are described and analyzed.

## 2 Navier-Stokes Equations

In general, the state of most fluids can be described by using the following macroscopic variables:

$\vec{u}$ ,	<i>fluid velocity</i>
$\rho$ ,	<i>fluid density</i>
$p$ ,	<i>pressure</i>
$T$ ,	<i>temperature</i>
$E$ ,	<i>energy</i>

The applicable governing equations for these variables can be derived from statistical mechanics using the microscopic equations of motion. Alternatively, they can be obtained through conservation laws. In divergence form, the conservation of mass (Eq. 1), momentum (Eq. 2), and energy (Eq. 3) can be expressed as:

$$\text{Mass: } \frac{\partial \rho}{\partial t} + \vec{\nabla} \cdot (\rho \vec{u}) = 0 \quad (1)$$

$$\text{Momentum: } \frac{\partial}{\partial t}(\rho \vec{u}) + \vec{\nabla} \cdot (\rho \vec{u} \vec{u} + p \mathbf{I} - \boldsymbol{\tau}) = \rho \vec{g} \quad (2)$$

$$\text{Energy: } \frac{\partial}{\partial t} E + \vec{\nabla} \cdot ((\rho E + p) \vec{u} - \kappa \vec{\nabla} T - (\vec{u} \cdot \boldsymbol{\tau})^T) = \rho(q + \vec{g} \cdot \vec{u}) \quad (3)$$

where:

$\vec{\nabla}$  = gradient operator  $\left( \frac{\partial}{\partial x_\alpha} \right)$

$\vec{g}$  = acceleration due to gravity

$q$  = internal heat source

$\kappa$  = thermal conductivity

$\mathbf{I}$  = identity matrix

$\boldsymbol{\tau}$  = deviatoric stress in the fluid.

For a Newtonian fluid,  $\boldsymbol{\tau}$  has the following form (Eq. 4):

$$\boldsymbol{\tau} = -\mu' \rho (\vec{\nabla} \cdot \vec{u}) \mathbf{I} + 2\rho\mu \mathbf{S} \quad (4)$$

Where  $\mu$  and  $\mu'$  represent the dynamic (shear) and bulk viscosity respectively, and  $\mathbf{S}$  (the strain rate tensor) is defined by Eq. 5:

$$\mathbf{S} = 1/2 \left( \vec{\nabla} \vec{u} + (\vec{\nabla} \vec{u})^T \right) \quad (5)$$

As written, for an  $n$ -dimensional space, Eq. 1–3 represent a system of  $n + 2$  equations for  $n + 4$  unknowns. To close the system, two additional equations of state are required: one relating the pressure and temperature and the other temperature and energy. For example, for a perfect gas, these equations are:  $p = \rho RT$  and  $E = C_v T$ , respectively.

## 2.1 Isothermal and incompressible flows

For an isothermal, incompressible flow, the effects of the temperature are neglected, and the density is assumed constant ( $\rho = \rho_0$ ). The conservation law for the mass is simplified and states that the velocity field is divergence free (solenoidal), shown by Eq. 6:

$$\vec{\nabla} \cdot \vec{u} = 0 \quad (6)$$

The conservation law for the momentum is also simplified and leads to the incompressible NS equations:

$$\partial_t \vec{u} + (\vec{u} \cdot \vec{\nabla}) \vec{u} = -\frac{1}{\rho_0} \vec{\nabla} p + \nu \nabla^2 \vec{u} \quad (7)$$

To find the value of pressure,  $p$ , one takes the divergence of Eq. 7. Making use of Eq. 6, this yields the Poisson equation (Eq. 8):

$$\nabla^2 p = -\rho_0 (\vec{\nabla} \vec{u}) : (\vec{\nabla} \vec{u})^T \quad (8)$$

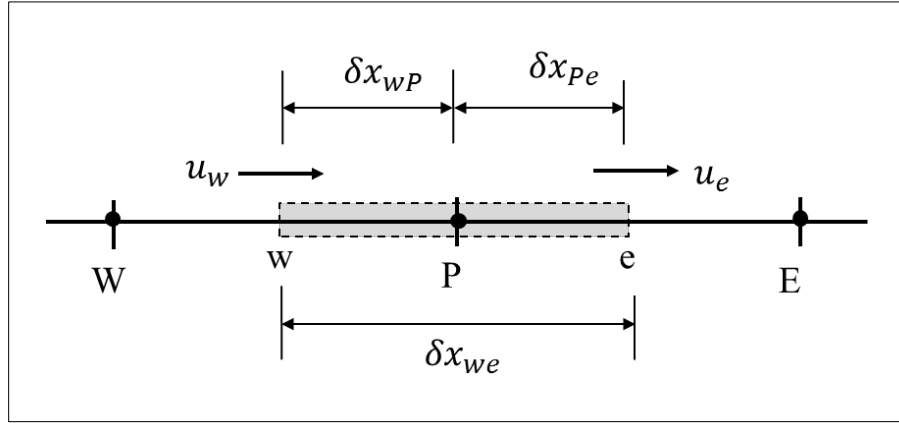
For implementation purposes, Eq. 8 is solved via an iterative procedure at each time step. The correct value of pressure is obtained in a way that ensures the velocity field remains divergence-free.

## 2.2 Finite volume discretization

While there are many methods that can be used to discretize the above conservation equations, for this work we implement the FVM (Versteeg and Malalasekera 1995). For illustration purposes, the FVM discretization pertaining to a steady-state flow involving one-dimensional convection

and diffusion of a quantity ( $\varphi$ ), is demonstrated for the control volume (Figure 1).

Figure 1. One-dimensional control volume used in the FVM.



For a diffusion coefficient ( $\Gamma$ ), Eq. 6 and Eq. 7 become:

$$\frac{d}{dx}(u) = 0 \quad (9)$$

$$\frac{d}{dx}(u\varphi) = \frac{d}{dx}\left(\Gamma \frac{d\varphi}{dx}\right) \quad (10)$$

Integration of Eq. 9 and Eq. 10 over the control volume gives us Eq. 11 and Eq. 12:

$$(uA\varphi)_e - (uA\varphi)_w = 0 \quad (11)$$

$$(uA\varphi)_e - (uA\varphi)_w = \left(\Gamma A \frac{d\varphi}{dx}\right)_e - \left(\Gamma A \frac{d\varphi}{dx}\right)_w \quad (12)$$

where:

$e$  and  $w$  represent directional indices as shown in Figure 1, and  $A$  is the control volume cross-sectional area.

As customary, we define the variables ( $F_e$ ,  $F_w$ , and  $D_e$ ,  $D_w$ ) to correspond to convection and diffusion in the east and west directions in Eq. 13 and Eq. 14, respectively:

$$F_e = (u)_e, \quad F_w = (u)_w \quad (13)$$

$$D_w = \frac{\Gamma_w}{\delta x_{WP}}, \quad D_e = \frac{\Gamma_e}{\delta x_{PE}} \quad (14)$$

Here the indices  $W$ ,  $P$ , and  $E$  correspond to the respective node locations shown in Figure 1.

Substituting Eq. 13 and Eq. 14 into Eq. 11 and Eq. 12, and assuming that all cross-sectional areas are equivalent (i.e.,  $A_w = A_e = A$ ), we have Eq. 15 and Eq. 16:

$$F_e - F_w = 0 \quad (15)$$

$$F_e \varphi_e - F_w \varphi_w = D_e (\varphi_E - \varphi_P) - D_w (\varphi_P - \varphi_W) \quad (16)$$

Finally, the convection terms on the left-hand side of Eq. 16 may be treated with an upwind differencing scheme, which takes into account the direction of the flow. For positive flows (streaming from left to right), we have Eq. 17:

$$\varphi_w = \varphi_W, \quad \text{and} \quad \varphi_e = \varphi_P \quad \text{for:} \quad u_w > 0, \text{ and } u_e > 0 \quad (17)$$

and for negative flows (right to left), we have Eq. 18:

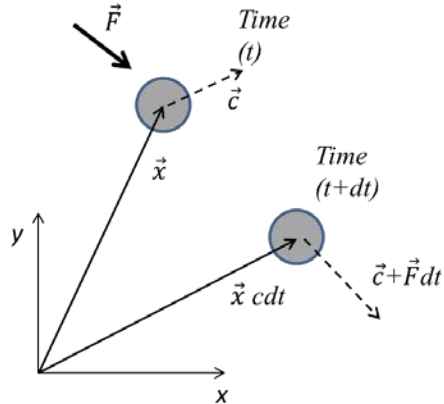
$$\varphi_w = \varphi_P, \quad \text{and} \quad \varphi_e = \varphi_E \quad \text{for:} \quad u_w < 0, \text{ and } u_e < 0 \quad (18)$$

This completes the discretization process for this simple, one-dimensional, convection-diffusion case.

### 3 Lattice Boltzmann Equation

As its name suggests, the Lattice Boltzmann (LB) equation may be regarded as a limited version of the generalized Boltzmann equation. The Boltzmann equation describes the phenomenological properties of particulate systems via the use of the phase space distribution function,  $f(\vec{x}, \vec{c}, t)$ . The phase space distribution function represents the number of particles at time  $t$ , positioned between  $\vec{x}$  and  $\vec{x} + d\vec{x}$ , with velocities between  $\vec{c}$  and  $\vec{c} + d\vec{c}$ . As shown in Figure 2, if we impose an external force ( $\vec{F}$ ) to a particle of unit mass, this force will result in a change in position and velocity, equivalent to:  $\vec{x} + \vec{c}dt$  and  $\vec{c} + \vec{F}dt$ , respectively.

Figure 2. Position and velocity vectors resulting from an external force.



For the idealized case in which there are no collisions between particles, we may equate the particle distribution at time  $(t)$  with that of time  $(t + dt)$ , to get Eq. 19:

$$f(\vec{x} + \vec{c}dt, \vec{c} + \vec{F}dt, t + dt)d\vec{x}d\vec{c} - f(\vec{x}, \vec{c}, t)d\vec{x}d\vec{c} = 0 \quad (19)$$

If collisions are included, it is clear that some particles, initially at  $(\vec{x}, \vec{c}, t)$ , will not arrive at  $(\vec{x} + \vec{c}dt, \vec{c} + \vec{F}dt, t + dt)$  simply because they have been diverted from their original path. Analytically, this may be represented as Eq. 20:

$$f(\vec{x} + \vec{c}dt, \vec{c} + \vec{F}dt, t + dt)d\vec{x}d\vec{c} - f(\vec{x}, \vec{c}, t)d\vec{x}d\vec{c} = \Omega(f)d\vec{x}d\vec{c}dt \quad (20)$$

where we have used  $\Omega(f)$  to represent the collision operator (physically representing the difference from the idealized streaming case). Dividing Eq. 20 by  $d\vec{x}d\vec{c}dt$  and taking the limit as  $dt \rightarrow 0$  yields Eq. 21:

$$\frac{df}{dt} = \Omega(f) \quad (21)$$

Since  $f$  is a function of  $\vec{x}$ ,  $\vec{c}$ , and  $t$ , the total rate of change of  $f$  may be written as Eq. 22:

$$df = (\vec{\nabla}_x f)d\vec{x} + (\vec{\nabla}_c f)d\vec{c} + \frac{\partial f}{\partial t}dt \quad (22)$$

Dividing by  $dt$  and applying Eq. 21, we obtain the familiar Boltzmann equation shown as Eq. 23 or Eq. 24:

$$\frac{df}{dt} = \frac{\partial f}{\partial t} + (\vec{\nabla}_x f)\vec{c} + (\vec{\nabla}_c f)\vec{F}/m = \Omega(f) \quad (23)$$

OR:

$$\frac{\partial f}{\partial t} + (\vec{c} \cdot \vec{\nabla}_x + \frac{\vec{F}}{m} \cdot \vec{\nabla}_c + \partial_t)f = \Omega(f) \quad (24)$$

Where  $\vec{\nabla}_x$  (for the two dimensional, Cartesian coordinate system shown in Figure 2) is  $(\frac{\partial}{\partial x}, \frac{\partial}{\partial y})$  and  $\nabla_c$  is  $(\frac{\partial}{\partial u}, \frac{\partial}{\partial v})$ .

The LB equation is easily derived from Eq. 24. By neglecting external forces ( $\vec{F}$ ), normalizing the mass to unity, and limiting the velocity ( $\vec{c}$ ) to a discrete set of vectors (in conformance with a prescribed lattice), the distribution function can be written as  $f_i(t, \vec{x})$  with no loss of information (Mohamad 2011). With time discretization, we have:  $\Omega dt \rightarrow \Omega_i(r, t)$ , and the LB equation can be written as Eq. 25:

$$f_i(t + \hat{\delta}_t, \vec{x} + \vec{c}_i \hat{\delta}_t) - f_i(\vec{x}, t) = \Omega_i(\vec{x}, t) \quad (25)$$

This equation has been written in lattice units, such that the time interval from one iteration to the next is  $\hat{\delta}_t$  and the spacing between two adjacent lattice nodes is  $\hat{\delta}_x$ , where  $\hat{\delta}_x = \vec{c}_i \hat{\delta}_t$ .

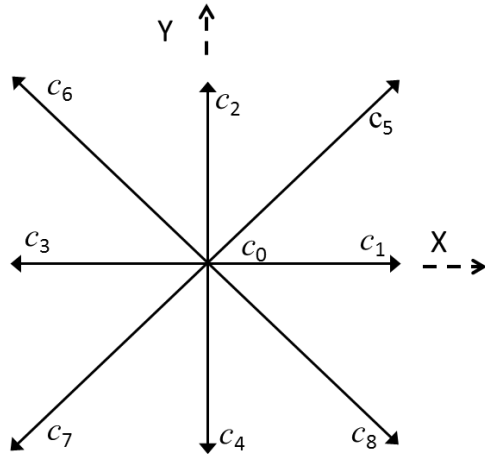
As stated previously, one of the main problems in solving the Boltzmann equation (Eq. 24) is the complicated nature of the integrodifferential colli-

sion term (Allen 2006) The current practice within the context of the LBM is to use the BGK relaxation approximation for the collision term (Higuera and Jimenez 1989; Koelman 1991). The BGK approximation involves relaxation dynamics (with relaxation parameter  $\omega$ ) towards local equilibrium, to produce Eq. 26:

$$\Omega_i^{BGK} = -\omega(f_i - f_i^{eq}) \quad (26)$$

As shown in Figure 3, the D2Q9 particle velocity model is used in this work (Qian et al. 1992). As shown, the particle velocities consist of a rest particle ( $c_0$ ) and eight moving particles ( $c_1, c_2, \dots, c_8$ ).

**Figure 3.** Lattice velocities corresponding to the D2Q9 configuration.



The local equilibrium distribution function ( $f_i^{eq}$ ) is obtained from a series approximation (see Appendix) and defined (up to second order) as Eq. 27:

$$f_i^{eq} = \hat{\rho} w_i \left[ 1 + \frac{c_{i\alpha} u_\alpha}{c_s^2} + \frac{(c_{i\alpha} u_\alpha)^2}{2c_s^4} - \frac{u^2}{2c_s^2} \right] \quad (27)$$

The speed of sound constant ( $c_s$ ) and the lattice weighting coefficients ( $w_i$ ) are determined such that a system of moment summations are satisfied. For a D2Q9 lattice configuration (Qian et al. 1992), these include Eq. 28–31):

$$\sum_i f_i^{eq} = \hat{\rho} \quad (28)$$

$$\sum_i f_i^{eq} c_{i\alpha} = \hat{\rho} u_\alpha \quad (29)$$

$$\sum_i f_i^{eq} c_{i\alpha} c_{i\beta} = \frac{1}{3} \hat{\rho} c_s^2 \delta_{\alpha\beta} + \hat{\rho} u_\alpha u_\beta \quad (30)$$

$$\sum_i f_i^{eq} c_{i\alpha} c_{i\beta} c_{iy} = \frac{1}{3} \hat{\rho} c_s^2 (\delta_{\alpha\beta} u_y + \delta_{\beta\delta} u_\alpha + \delta_{y\alpha} u_\beta) \quad (31)$$

Where the subscript indices ( $\alpha, \beta, \dots$ ) represent the spatial components of the vectors,  $c_s$  is the lattice speed of sound, and  $\delta$  is the Kronecker delta.

Satisfying Eq. 28-31, a value of  $c_s^2 = 1/3$  is often used, with weighting coefficients as shown in Eq. 32:

$$w_i = \frac{4}{9} (i = 0), \quad w_i = \frac{1}{9} (i = 1,2,3,4), \quad \text{and } w_i = \frac{1}{36} (i = 5,6,7,8) \quad (32)$$

The macroscopic density ( $\hat{\rho}$ ) and velocity ( $u_\alpha$ ) are calculated from moment summations using the distribution function, as shown in Eq. 33 and Eq. 34, respectively:

$$\hat{\rho} = \sum_i f_i \quad (33)$$

$$\hat{\rho} u_\alpha = \sum_i f_i c_{i\alpha} \quad (34)$$

## 4 Lattice Boltzmann/Navier-Stokes Equivalence using the Chapman-Enskog Expansion

Under the assumption of negligible density fluctuations (e.g., incompressible flow), the Chapman-Enskog expansion (Chapman and Cowling 1970) can be used to show LBM equivalence to the NS equations. To summarize, the basic idea behind the Chapman-Enskog expansion is to separate the distribution function into multiple scales with respect to the order of Knudsen number ( $\epsilon$ ). Physical properties of the macroscopic variables, such as the density and momentum, are automatically separated out from the different scales.

In detail, the process begins first with the distribution function written as an asymptotic series expanded over the Knudsen number ( $\epsilon$ ), as in Eq. 35:

$$f_i = f_i^{(0)} + \epsilon f_i^{(1)} + \epsilon^2 f_i^{(2)} + \dots \quad (35)$$

The functions ( $f_i^{(k)}$ ) are defined in such a way as to progressively and independently tend toward zero with increasing powers of epsilon (which necessarily assumes that epsilon is a very small quantity consistent with the continuum assumption). Since the main objective of the Chapman-Enskog expansion is to provide a consistent definition for  $f_i^{(k)}$ , preliminarily this means satisfying Eq. 33 and Eq. 34 as Eq. 36 and Eq. 37 by requiring that the first two moments of the zeroth approximation reproduce macroscopic density and velocity. The corresponding moments of the higher-order terms are set to zero:

$$\sum_i f_i^{(0)} = \hat{\rho}; \quad \sum_i f_i^{(0)} c_{i\alpha} = \hat{\rho} u_\alpha \quad (36)$$

$$\sum_i f_i^{(k)} = 0; \quad \sum_i f_i^{(k)} c_{i\alpha} = 0; \quad \text{for } k > 0 \quad (37)$$

Using the BGK approximation, the LB equation may be written as Eq. 38:

$$f_i(t + \Delta t, \vec{x} + \vec{c}_i \delta_t) - f_i(t, \vec{x}) = -\frac{1}{\tau} [f_i(t, \vec{x}) - f_i^{eq}(t, \vec{x})], \quad (i = 0 \dots N) \quad (38)$$

Applying a Taylor series expansion ( $t, \vec{x}$ ) to the first term of Eq. 38 yields Eq. 39:

$$f_i(t + \delta_t, \vec{x} + \vec{c}_t \delta_t) = f_i + \delta_t \left( \frac{\partial}{\partial t} + c_{i\alpha} \frac{\partial}{\partial x_\alpha} \right) f_i + \frac{\delta_t^2}{2} \left( \frac{\partial}{\partial t} + c_{i\alpha} \frac{\partial}{\partial x_\alpha} \right)^2 f_i + O(\delta_t^3) \quad (39)$$

Where  $f_i(t, \vec{x})$  is simplified to  $f_i$  for convenience, and:

$$\left( \frac{\partial}{\partial t} + c_{i\alpha} \frac{\partial}{\partial x_\alpha} \right)^2 f_i \equiv \left( \frac{\partial^2}{\partial t^2} + 2c_{i\alpha} \frac{\partial^2}{\partial t \partial x_\alpha} + c_{i\alpha} c_{i\beta} \frac{\partial^2}{\partial x_\alpha \partial x_\beta} \right) f_i \quad (40)$$

Substituting Eq. 39 into Eq. 38 and dividing by  $\delta_t$  yields Eq. 41:

$$\left( \frac{\partial}{\partial t} + c_{i\alpha} \frac{\partial}{\partial x_\alpha} \right) f_i + \frac{\delta_t}{2} \left( \frac{\partial}{\partial t} + c_{i\alpha} \frac{\partial}{\partial x_\alpha} \right)^2 f_i + \frac{1}{\delta_t \tau} (f_i - f_i^{eq}) = O(\delta_t^2) \quad (41)$$

Since  $\epsilon$  and  $\delta_t$  are approximately the same magnitude (for  $c_s = O(1)$ ), the distribution function  $f_i$  can be expanded in the asymptotic series shown in Eq. 42:

$$f_i = f_i^{eq} + \delta_t f_i^{(1)} + \delta_t^2 f_i^{(2)} + \dots \quad (42)$$

Inserting Eq. 4) into Eq. 41, we have Eq. 43:

$$\begin{aligned} & \left( \frac{\partial}{\partial t} + c_{i\alpha} \frac{\partial}{\partial x_\alpha} \right) (f_i^{eq} + \delta_t f_i^{(1)} + \delta_t^2 f_i^{(2)} + \dots) \\ & + \frac{\delta_t}{2} \left( \frac{\partial}{\partial t} + c_{i\alpha} \frac{\partial}{\partial x_\alpha} \right)^2 (f_i^{eq} + \delta_t f_i^{(1)} + \delta_t^2 f_i^{(2)} + \dots) \\ & + \frac{1}{\delta_t \tau} (f_i^{eq} + \delta_t f_i^{(1)} + \delta_t^2 f_i^{(2)} + \dots - f_i^{eq}) = O(\delta_t^2) \end{aligned} \quad (43)$$

Organizing terms according to the order of  $\delta_t$  we have Eq. 44:

$$\begin{aligned} & \left[ \left( \frac{\partial}{\partial t} + c_{i\alpha} \frac{\partial}{\partial x_\alpha} \right) f_i^{eq} + \frac{1}{\tau} f_i^{(1)} \right] \\ & + \delta_t \left[ \left( \frac{\partial}{\partial t} + c_{i\alpha} \frac{\partial}{\partial x_\alpha} \right) f_i^{(1)} + \frac{1}{2} \left( \frac{\partial}{\partial t} + c_{i\alpha} \frac{\partial}{\partial x_\alpha} \right)^2 f_i^{eq} + \frac{1}{\tau} f_i^{(2)} \right] = O(\delta_t^2) \end{aligned} \quad (44)$$

To obtain the Euler expression (the inviscid form of NS), the first term of Eq. 44 is assumed zero, creating Eq. 45:

$$\left( \frac{\partial}{\partial t} + c_{i\alpha} \frac{\partial}{\partial x_\alpha} \right) f_i^{eq} + \frac{1}{\tau} f_i^{(1)} = 0 \quad (45)$$

Taking the summation  $\sum_i$  on Eq. (45) and using Eq. 28, Eq. 29, and Eq. 36, we obtain the equation for the conservation of mass in Eq. 46:

$$\begin{aligned} & \sum_i \left[ \left( \frac{\partial}{\partial t} + c_{i\alpha} \frac{\partial}{\partial x_\alpha} \right) f_i^{eq} + \frac{1}{\tau} f_i^{(1)} \right] \\ &= \frac{\partial}{\partial t} \sum_i f_i^{eq} + \frac{\partial}{\partial x_\alpha} \sum_i f_i^{eq} c_{i\alpha} + \frac{1}{\tau} \sum_i f_i^{(1)} \\ &= \frac{\partial}{\partial t} \rho + \frac{\partial}{\partial x_\alpha} (\rho u_\alpha) = 0 \end{aligned} \quad (46)$$

Taking the summation  $\sum_i c_{i\alpha}$  on Eq. 45 and using Eq. 29, Eq. 30, and Eq. 37, we obtain Euler's equation for the conservation of momentum (Eq. 48):

$$\begin{aligned} & \sum_i c_{i\alpha} \left[ \left( \frac{\partial}{\partial t} + c_{i\beta} \frac{\partial}{\partial x_\beta} \right) f_i^{eq} + \frac{1}{\tau} f_i^{(1)} \right] \\ &= \frac{\partial}{\partial t} \sum_i f_i^{eq} c_{i\alpha} + \frac{\partial}{\partial x_\beta} \sum_i f_i^{eq} c_{i\alpha} c_{i\beta} + \frac{1}{\tau} \sum_i f_i^{(1)} c_{i\alpha} \\ &= \frac{\partial}{\partial t} (\rho u_\alpha) + \frac{\partial}{\partial x_\beta} \left( \frac{1}{3} \rho c^2 \delta_{\alpha\beta} + \rho u_\alpha u_\beta \right) = 0 \end{aligned} \quad (47)$$

Next the contribution from the second term of Eq. (44) is evaluated. Applying the differential operation  $\left( \frac{\partial}{\partial t} + c_{i\alpha} \frac{\partial}{\partial x_\alpha} \right)$  on Eq. (45) we have Eq. 48:

$$\left( \frac{\partial}{\partial t} + c_{i\alpha} \frac{\partial}{\partial x_\alpha} \right)^2 f_i^{eq} + \frac{1}{\tau} \left( \frac{\partial}{\partial t} + c_{i\alpha} \frac{\partial}{\partial x_\alpha} \right) f_i^{(1)} = 0 \quad (48)$$

Inserting Eq. 48 into the second term of Eq. 44 to eliminate the squared differentiation results in Eq. 49:

$$\begin{aligned} \delta_t & \left[ \left( \frac{\partial}{\partial t} + c_{i\alpha} \frac{\partial}{\partial x_\alpha} \right) f_i^{(1)} + \frac{1}{2} \left( \frac{\partial}{\partial t} + c_{i\alpha} \frac{\partial}{\partial x_\alpha} \right)^2 f_i^{eq} + \frac{1}{\tau} f_i^{(2)} \right] \\ & = \delta_t \left[ \left( 1 - \frac{1}{2\tau} \right) \left( \frac{\partial}{\partial t} + c_{i\alpha} \frac{\partial}{\partial x_\alpha} \right) f_i^{(1)} + \frac{1}{\tau} f_i^{(2)} \right] \end{aligned} \quad (49)$$

Taking the summation  $\sum_i$  on Eq. 49 and using Eqs. 36 and 37, we have Eq. 50:

$$\begin{aligned} & \sum_i \delta_t \left[ \left( 1 - \frac{1}{2\tau} \right) \left( \frac{\partial}{\partial t} + c_{i\alpha} \frac{\partial}{\partial x_\alpha} \right) f_i^{(1)} + \frac{1}{\tau} f_i^{(2)} \right] \\ & = \delta_t \left[ \left( 1 - \frac{1}{2\tau} \right) \left( \frac{\partial}{\partial t} \sum_i f_i^{(1)} + \frac{\partial}{\partial x_\alpha} \sum_i f_i^{(1)} c_{i\alpha} \right) + \frac{1}{\tau} \sum_i f_i^{(2)} \right] = 0 \end{aligned} \quad (50)$$

Taking the summation  $\sum_i c_{i\alpha}$  on Eq. (49) and inserting Eq. 37 yields Eq. 51:

$$\begin{aligned} & \sum_i c_{i\alpha} \delta_t \left[ \left( 1 - \frac{1}{2\tau} \right) \left( \frac{\partial}{\partial t} + c_{i\beta} \frac{\partial}{\partial x_\beta} \right) f_i^{(1)} + \frac{1}{\tau} f_i^{(2)} \right] \\ & = \Delta t \left[ \left( 1 - \frac{1}{2\tau} \right) \left( \frac{\partial}{\partial t} \sum_i f_i^{(1)} c_{i\alpha} + \frac{\partial}{\partial x_\beta} \sum_i f_i^{(1)} c_{i\alpha} c_{i\beta} \right) + \frac{1}{\tau} \sum_i f_i^{(2)} c_{i\alpha} \right] \\ & = \delta_t \left( 1 - \frac{1}{2\tau} \right) \frac{\partial}{\partial x_\beta} \sum_i f_i^{(1)} c_{i\alpha} c_{i\beta} \end{aligned} \quad (51)$$

From Eq. 45, the distribution  $f_i^{(1)}$  is shown in Eq. 52:

$$f_i^{(1)} = -\tau \left( \frac{\partial}{\partial t} + c_{i\beta} \frac{\partial}{\partial x_\beta} \right) f_i^{eq} \quad (52)$$

Therefore the term  $\sum_i f_i^{(1)} c_{i\alpha} c_{i\beta}$  in Eq. 51 is transformed to Eq. 53, using Eq. 30 and Eq. 31:

$$\begin{aligned} & \sum_i f_i^{(1)} c_{i\alpha} c_{i\beta} = -\tau \sum_i \left( \frac{\partial}{\partial t} + c_{i\gamma} \frac{\partial}{\partial x_\gamma} \right) f_i^{(eq)} c_{i\alpha} c_{i\beta} \\ & = -\tau \left[ \frac{\partial}{\partial t} \left( \frac{1}{3} \rho c^2 \delta_{\alpha\beta} + \rho u_\alpha u_\beta \right) + \frac{\partial}{\partial x_\gamma} \left( \frac{1}{3} \rho c^2 (\delta_{\alpha\beta} u_\gamma + \delta_{\beta\gamma} u_\alpha + \delta_{\gamma\alpha} u_\beta) \right) \right] \\ & = -\tau \left[ \frac{1}{3} c^2 \delta_{\alpha\beta} \frac{\partial}{\partial t} \rho + \frac{\partial}{\partial t} (\rho u_\alpha u_\beta) + \frac{\partial}{\partial x_\gamma} \left( \frac{1}{3} \rho c^2 (\delta_{\alpha\beta} u_\gamma + \delta_{\beta\gamma} u_\alpha + \delta_{\gamma\alpha} u_\beta) \right) \right] \end{aligned} \quad (53)$$

Applying the product rule to the term  $\frac{\partial}{\partial t}(\rho u_\alpha u_\beta)$  of Eq. 53 yields Eq. 54:

$$\frac{\partial}{\partial t}(\rho u_\alpha u_\beta) = u_\beta \frac{\partial}{\partial t}(\rho u_\alpha) + u_\alpha \frac{\partial}{\partial t}(\rho u_\beta) + u_\alpha u_\beta \frac{\partial}{\partial t}\rho \quad (54)$$

Using Eq. 46 and Eq. 47 for  $\frac{\partial}{\partial t}\rho$  and  $\frac{\partial}{\partial t}(\rho u_\alpha)$ , respectively, we have Eq. 55:

$$\sum_i f_i^{(1)} c_{i\alpha} c_{i\beta} = -\tau \left[ \frac{1}{3} \rho c^2 \left( \frac{\partial u_\alpha}{\partial x_\beta} + \frac{\partial u_\beta}{\partial x_\alpha} \right) - \frac{\partial}{\partial x_\gamma} (\rho u_\alpha u_\beta u_\gamma) \right] \quad (55)$$

Summing Eq. 47 and Eq. 51 with Eq. 55 and neglecting  $\frac{\partial}{\partial x_\gamma}(\rho u_\alpha u_\beta u_\gamma)$  as a small quantity results in the momentum equation (Eq. 56) in the NS equations:

$$\begin{aligned} & \frac{\partial}{\partial t}(\rho u_\alpha) + \frac{\partial}{\partial x_\alpha} \left( \frac{1}{3} \rho c^2 \right) + \frac{\partial}{\partial x_\beta} (\rho u_\alpha u_\beta) \\ & - \frac{\partial}{\partial x_\beta} \left[ \delta_t \left( \tau - \frac{1}{2} \right) \frac{1}{3} \rho c^2 \left( \frac{\partial u_\alpha}{\partial x_\beta} + \frac{\partial u_\beta}{\partial x_\alpha} \right) \right] = 0 \end{aligned} \quad (56)$$

Where the pressure ( $P$ ) and viscosity ( $\mu$ ) are expressed as Eq. 57 and Eq. 58, respectively:

$$P = \frac{1}{3} \rho c^2 \quad (57)$$

$$\mu = \delta_t \left( \tau - \frac{1}{2} \right) \frac{1}{3} \rho c^2 \quad (58)$$

## 5 Implementation Issues

As shown in the previous section, the incompressible NS equations can be derived from the LB equation through the Chapman-Enskog procedure *if the density fluctuation is assumed negligible*. In practice however, this last assumption is never completely true. Indeed, the spatial density variation is never completely zero in LBM simulations. This is particularly true for flow applications wherein a pressure gradient is imposed at the boundaries. Although there have been recent efforts to reduce or completely eliminate the compressible effect in the LBM, the results have not been entirely satisfactory, particularly for unsteady flows (Frisch et al. 1987; Alexander et al. 1992; Zou et al. 1995).

Despite its intrinsic compressibility, the LBM is applicable only to the low Mach number ( $Ma = u/c_s$ ) flow applications. As shown in the previous section, this is because a small velocity expansion is (*implicitly*) used within the Chapman-Enskog expansion. This low Mach number approximation is equivalent to the incompressible limit (i.e.,  $Ma < 0.3$ ).

To correctly simulate incompressible flow in practice, one must ensure that the Mach number, and the density variation,  $\delta p$ , are sufficiently small, of order  $O(\epsilon)$  and  $O(\epsilon^2)$ , respectively, where the Knudsen number may be approximated as  $\epsilon = (c\tau)/L$ . Quantitatively, this can be assured from the expression of the Mach number as a function of the Reynolds number. Since the fluid viscosity is related to the relaxation frequency ( $\omega = 1/\tau$ ), we have Eq. 59:

$$\nu = \frac{\hat{\delta}_x^2}{3\hat{\delta}_t} (\omega - 0.5) \quad (59)$$

The Mach number,  $Ma$ , can be obtained by dividing both sides of equation x by  $UL$ . This action yields Eq. 60:

$$Ma = \frac{\hat{\delta}_x}{L\sqrt{3}} (\omega - 0.5) Re \quad (60)$$

In Eq. 60  $\hat{L}/\hat{\delta}_x$  is the number of lattice sites,  $N$ , in the direction of the characteristic length (normally perpendicular to the flow direction), and  $Re$  is the Reynolds number ( $Re = \hat{U}N/\hat{\nu}$ ). Since  $\hat{\delta}_x$  is normally assigned a

value of unity (for purposes of convenience) to keep  $Ma$  small ( $Ma < 0.3$ ), then  $\omega$ ,  $N$ , and  $\widehat{U}$  should be selected accordingly. In practice,  $\widehat{U}$  is generally prescribed values on the order of 0.1. Since Reynolds number similarity must also be enforced between the macroscale and lattice environments, this enforcement places an additional constraint on the selection of  $\omega$  and  $N$ .

In addition to the aforementioned constraints, additional stability issues may arise due to the presence of parasitic oscillations in the vicinity of sharp gradients in the flow. These sharp gradients may be caused by shock waves travelling through the fluid or by excessively thin shear layers.

While conventional methods allow for a certain amount of numerical, artificial diffusion to mitigate impending instabilities of this sort, this mitigation is not the case for the traditional LBM. Indeed, as shown in Eq. 26, the traditional BGK collision approximation involves only a single, constant-valued relaxation time. While several novel “dissipative” methods have recently attempted to address this stabilization issue, including collision operations involving multiple relaxation times (MRTs) (d’Humieres 1994; d’Humieres et al. 2002), these methods have demonstrated only limited success. This lack of success is largely due to the fact that although the dissipative methods can provide substantial (or complete) oscillatory suppression, accuracy is compromised. However, due to the low Mach number used in this work in incompressible flow restraints, this type of stability issue is of negligible concern.

## 6 Lattice Boltzmann and Navier-Stokes Benchmark Applications

The following benchmark applications were selected for their ubiquity in the scientific and engineering literature, relative ease to set-up, and computational efficiency. All of the simulations were run in two dimensions and in serial using a Dell Precision 490 desktop machine with two Dual-Core Xeon 64 bit processors. Post processing was facilitated using VTK<sup>\*</sup>-formatted output files and Paraview<sup>†</sup> (Henderson 2007).

The Navier-Stokes simulations were conducted using the finite volume solver, OpenFOAM version 2.1.<sup>‡</sup> In particular, the incompressible laminar flow equations (Eq. 6-8) were solved in conjunction with the pressure implicit with splitting operator (PISO) algorithm (Issa 1986). Discretization of diffusion and convective terms was carried out using standard second-order central differencing and upwinding schemes, respectively. Since the OpenFOAM code is inherently transient, steady-state conditions were obtained over extended time periods, as quantified by residual values of less than  $10^{-6}$ . Specifically, the steady-state condition was checked by calculating the residual (*Res*) of the x-component of velocity at each time step, in accordance with the following equation:

$$Res = \sum_{y=1}^{LY} \sum_{x=1}^{LX} \left( \frac{|u(x,y)_{t+1} - u(x,y)_t|}{|u(x,y)_{t+1}|} \right) \quad (61)$$

The LBM code routines were developed in-house by ERDC and programmed in FORTRAN 90 using much of the prescribed content in Chapter 3. Collaborations with Mississippi State University's Center for

<sup>\*</sup> The Visualization Toolkit (VTK) is an open-source, freely available software system for 3D computer graphics, image processing and visualization.

<sup>†</sup> Paraview is an open-source multiple-platform application for interactive, scientific visualization, which began in 2000 as a collaborative effort between Kitware and Los Alamos National Laboratory.

<sup>‡</sup> OpenFOAM is a free, open-source computational fluid dynamics software developed by OpenCFD Ltd. of the ESI Group and distributed by the Open Foam Foundation. More information is available at [openfoam.org/version 2.1.1](http://openfoam.org/version 2.1.1).

Advanced Vehicular Systems (CAVS) were of significant benefit in the code development process. A two-dimensional square lattice with nine lattice velocities (D2Q9) was used (Qian et al. 1992). Boundary conditions (in particular the bounce back, velocity inlet/outlet conditions, and pressure conditions), were implemented in accordance with those prescribed by Zou and He (1997). In addition to the standard LBM, the implementation of the IMB method (Owen et al. 2011) was also incorporated for the case of the flow over a circular cylinder. Implemented in accordance with Owen et al. (2011), this method better represents the intersection of the fluid with the curved cylinder walls. While the exact details are omitted in this report for reasons of scope, Eq. 62–65 outline the basic procedure.

The standard LBM equation (Eq. 38) is modified according to Eq. 62:

$$f_i(\vec{x} + \vec{e}_i \delta t, t + \delta t) - f_i(\vec{x}, t) = (1 - B_n) \left( \frac{\delta t}{\tau} \left( f_i^{eq}(\vec{x}, t) - f_i(\vec{x}, t) \right) \right) + B_n \Omega_i^s \quad (62)$$

Where  $B_n$  is an empirically derived weighting function of the area (or volume) fraction ( $\varepsilon$ ) of lattice cell ( $i$ ) that is occupied by the cylinder, the result is Eq. 63:

$$B_n(\varepsilon) = \frac{\varepsilon(\tau-1/2)}{(1-\varepsilon)+(\tau-1/2)} \quad (63)$$

Where  $\Omega_i^s$  is a collision operator representing the change of momentum due to collisions with the cylinder, we have Eq. 64:

$$\Omega_i^s = [f_{i'}(\vec{x}, t) - f_{i'}^{eq}(\rho, \vec{v}_p)] - [f_i(\vec{x}, t) - f_i^{eq}(\rho, \vec{v}_p)] \quad (64)$$

Where  $i'$  represents the direction opposite  $\vec{e}_i$ , and  $\vec{v}_p$  is the velocity at the surface of the cylinder at point  $p$  (located at close proximity to lattice node  $i$ ), we have Eq. 65:

$$\vec{v}_p = \vec{v}_{cm} + \vec{\omega} \times \vec{r}_{p/cm} \quad (65)$$

Where  $\vec{v}_{cm}$  is the velocity of the cylinder's center of mass,  $\vec{\omega}$  is the angular velocity, and  $\vec{r}_{p/cm}$  is the position vector at  $p$  relative to the center of mass of the cylinder.

## 6.1 Rectangular channel flow

### 6.1.1 Problem description and setup

The incompressible flow through a rectangular channel represents a common computational fluid dynamics (CFD) benchmark problem. The flow is typically driven by either a constant inlet velocity condition or by means of a pressure gradient. In this particular application, water flows between two parallel plates of length ( $L = 0.5\text{ m}$ ), height ( $H = 0.02\text{ m}$ ) and of aspect ratio,  $AR = 25$ . Prescribed velocity /pressure gradient conditions are applied at the inlet and outlet boundaries, while no-slip (zero velocity) conditions are applied along the walls.

For the velocity inlet condition, three different Reynolds numbers are investigated using both the LB and NS methods. These cases correspond to  $Re=200$ ,  $Re=400$ , and  $Re=800$ . The pressure gradient condition is also examined using both methods, but only for  $Re = 10$ . The corresponding input parameters are shown in Table 1, with a constant lattice/grid resolution of 1000x40 maintained throughout.

Table 1. Simulation parameters used for the rectangular channel flow problem.

Case	Inlet Vel. ( $U_{in}$ ), Nav-Stokes [m/s]	Inlet Vel. ( $U_{lat}$ ) LB [ $\hat{l}/\hat{t}$ ]	Kin. Visc. ( $\nu$ ), Nav-Stokes [m <sup>2</sup> /s]	Kin. Visc. ( $\hat{\nu}$ ), LB [ $\hat{l}^2/\hat{t}$ ]	$\Delta P$
$Re = 10$	—	—	1.0E-6	0.16667	1.0E-5
$Re = 200$	0.01	0.3	1.0E-6	0.01	—
$Re = 400$	0.02	0.2	1.0E-6	0.02	—
$Re = 800$	0.04	0.1	1.0E-6	0.01	—

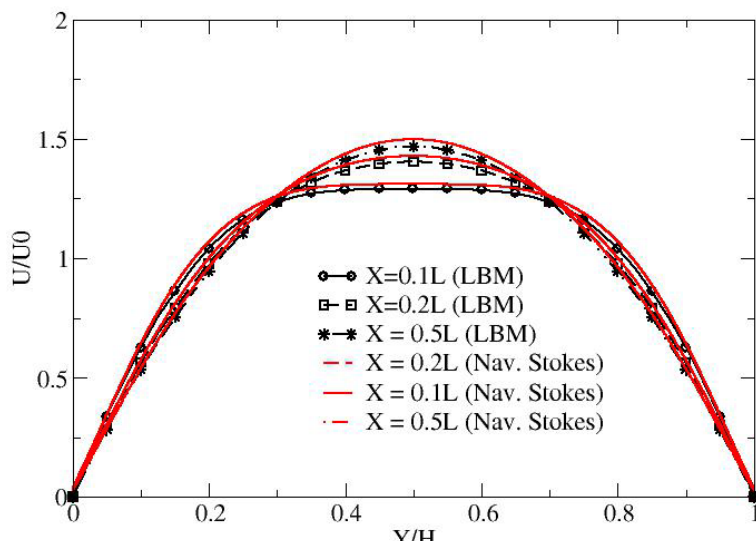
### 6.1.2 Results

The velocity profiles comparing the results of the LBM and NS method when using various velocity inlet conditions are shown in Figure 4. As expected, the velocity distribution along the downstream direction progressively evolves into a characteristic parabolic profile as the flow reaches a state of steady equilibrium. Also as expected, increasing the Reynolds number results in higher velocity profiles along each of the downstream positions ( $X/H = 0.1L$ ,  $X/H=0.2L$ , and  $X/H=0.5L$ ). Comparisons between the LBM and NS methods show excellent agreement.

The velocity profiles comparing the results of the LBM and NS method when using a pressure gradient boundary condition are shown in Figure 5. Unlike Figure 4, the imposed pressure gradient results in a uniform velocity distribution along each of the downstream sampling locations. Like Figure 4, the comparisons between the LBM and NS methods again show excellent agreement.

Finally, Figure 6 shows a representative time history of the convergence error in accordance with Eq. 61. As indicated, the residual for x-component of velocity becomes fully convergent (reaches a steady-state condition) at approximately 2,000 iterations.

**Figure 4.** Velocity profiles comparing the results of the LBM and NS corresponding to the flow through a rectangular channel (a)  $Re = 200$ , (b)  $Re = 400$ , and (c)  $Re = 800$ . A velocity inlet condition is used. As indicated, the velocities were sampled at three downstream locations corresponding to  $X/L = 0.1$ ,  $X/L = 0.2$  and  $X/L = 0.5$ . (Lattice/grid resolution = 1000x40).



(a)  $Re = 200$

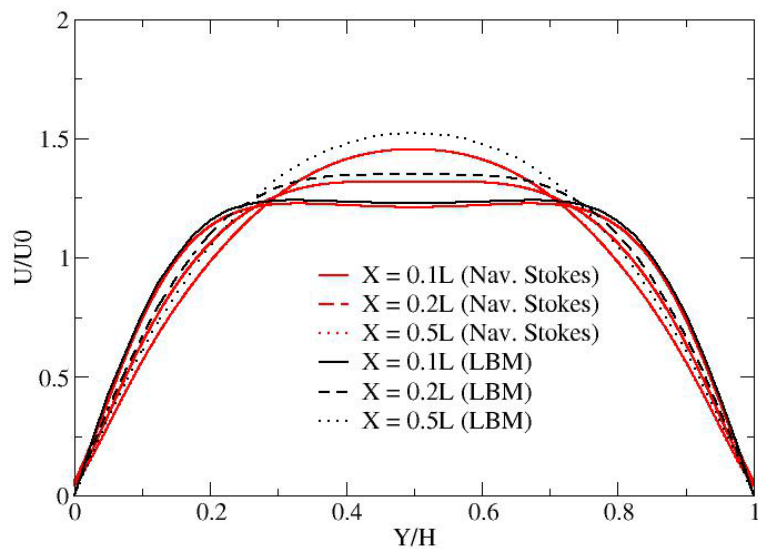
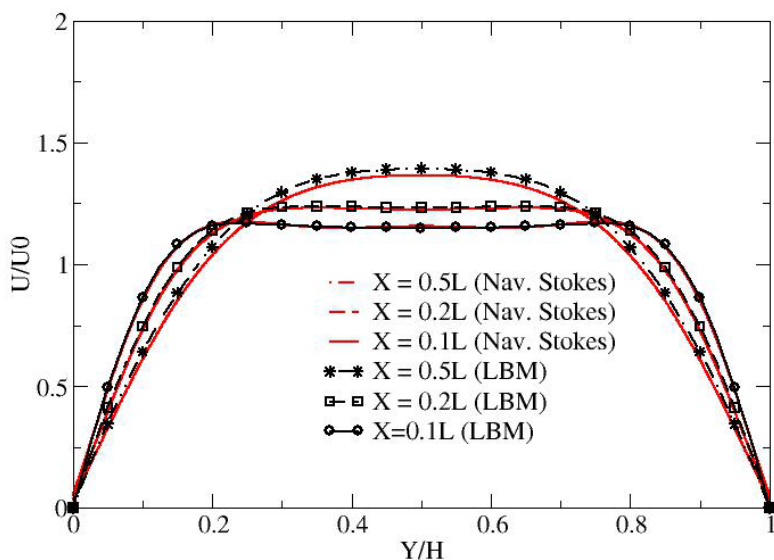
(b)  $Re = 400$ (c)  $Re = 800$

Figure 5. Velocity profiles comparing the results of the LBM and NS corresponding to the flow through a rectangular channel ( $Re = 200$ ,  $Re = 400$ , and  $Re = 800$ ). A pressure gradient condition is used. As indicated, the velocities were sampled at three downstream locations corresponding to  $X/L = 0.1$ ,  $X/L = 0.2$  and  $X/L = 0.5$ . (Lattice/grid resolution = 1,000x40).

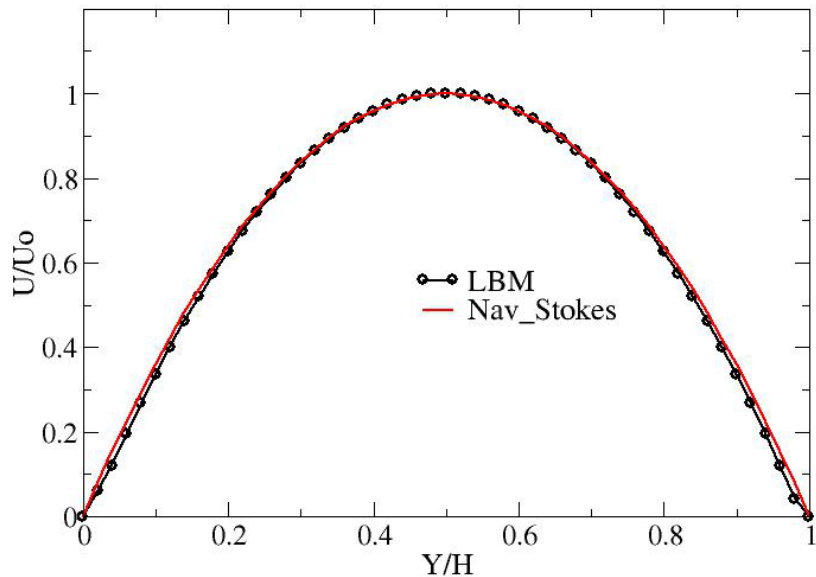
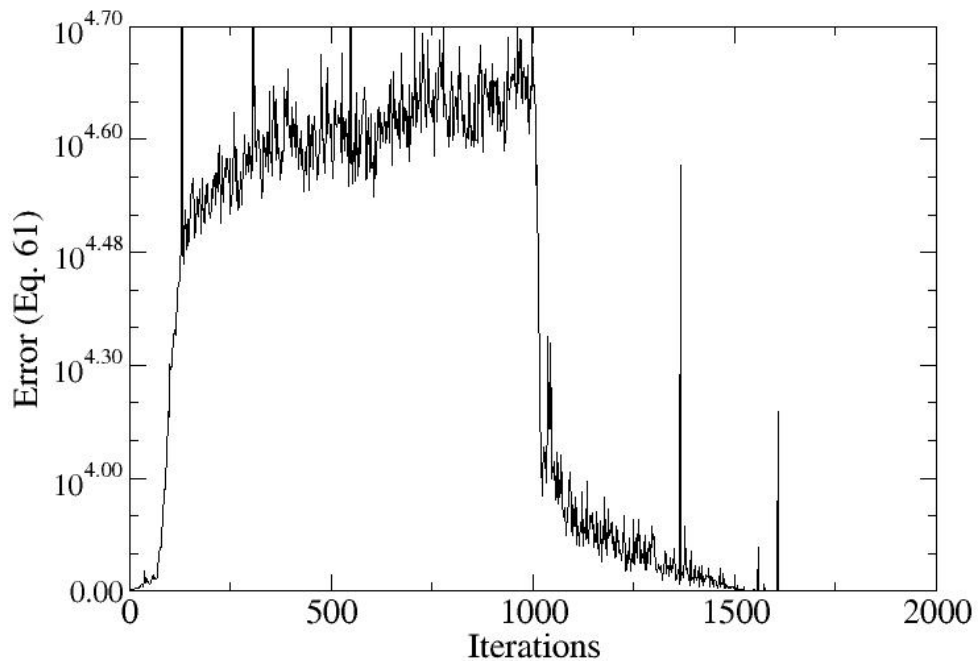


Figure 6. Representative velocity convergence error per Eq. 61 for the flow through a rectangular channel. As shown, approximately 2,000 LBM iterations were required for fully steady-state conditions.



## 6.2 Flow through a lid-driven cavity

### 6.2.1 Problem description and setup

The lid-driven cavity represents another common CFD benchmark problem. The moving lid creates a strong vortex in the center of the domain, and a series of weaker, secondary vortices in the lower left and right corners are typical of successively higher Reynolds numbers. In this particular application, a square cavity with unit aspect ratio ( $L = H = 2m$ ) is filled with engine oil at 15°C ( $\nu = 1.2\text{E-}3 \text{ m}^2/\text{s}$ ). The lid is set in motion (providing a fluid momentum source), and zero velocity (no-slip) boundary conditions are maintained along the remaining walls.

For this problem, three different Reynolds numbers are investigated ( $Re=100$ ,  $Re=1,000$ , and  $Re=3,000$ ), and the corresponding input parameters are shown in Table 2 for both the LBM and NS methods. A constant lattice/grid resolution of 100x100 is maintained for each case.

Table 2. Simulation parameters used for lid-driven cavity problem.

Case	Lid Vel. ( $U_{lid}$ ), Nav-Stokes [m/s]	Inlet Vel. ( $U_{lat}$ ) LB [ $\hat{l}/\hat{t}$ ]	Kin. Visc. ( $\nu$ ), Nav- Stokes [ $\text{m}^2/\text{s}$ ]	Kin. Visc. ( $\hat{\nu}$ ), LB [ $\hat{l}^2/\hat{t}$ ]
$Re = 100$	0.6	0.1	1.2E-3	0.1
$Re = 1000$	6	0.1	1.2E-3	0.01
$Re = 3000$	18	0.01	1.2E-3	0.01

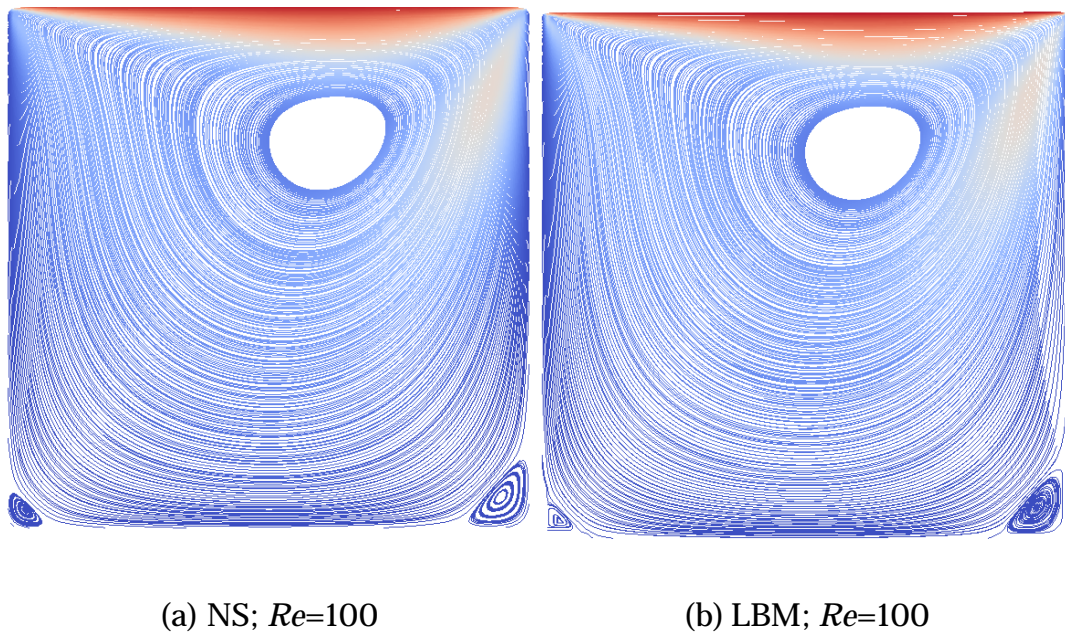
### 6.2.2 Results

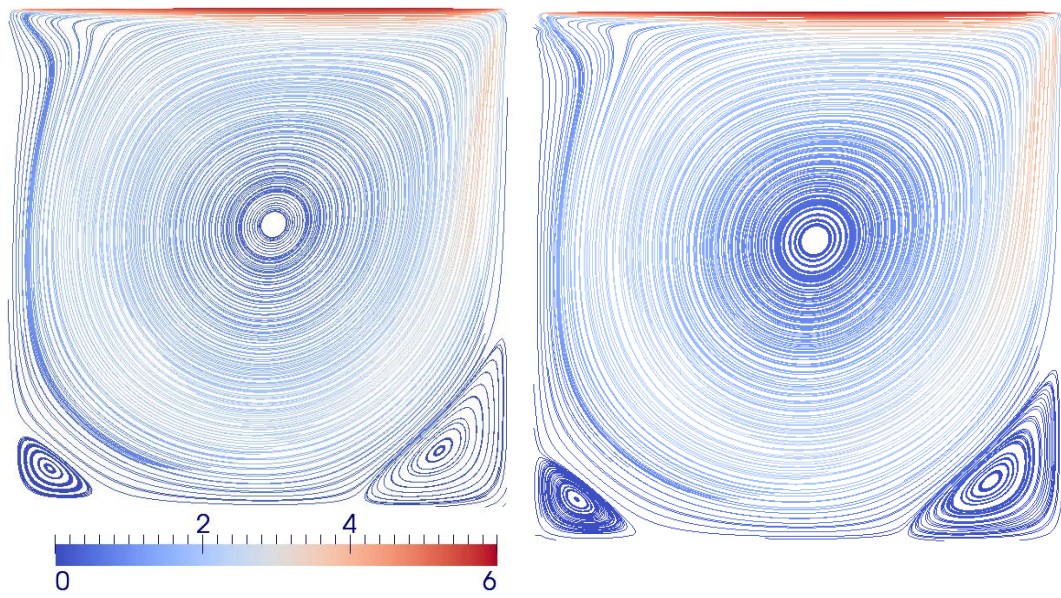
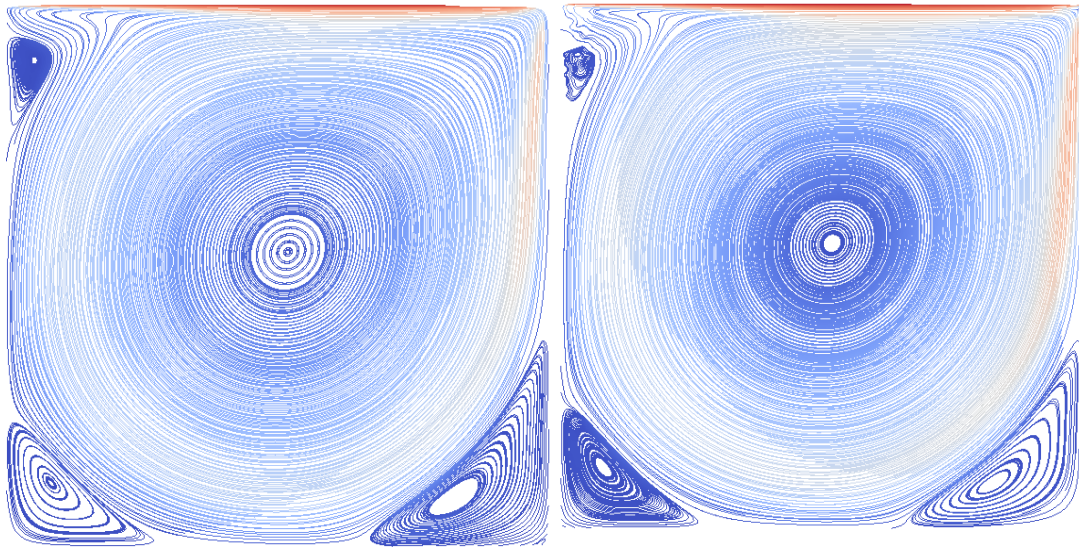
Comparisons of the velocity contours are shown in Figure 7. As indicated for the prescribed simulated conditions, both methods show remarkable qualitative agreement and reveal the presence of a large central vortex which tends to migrate to the upper right corner for decreasing Reynolds numbers. Also observed is the presence of two secondary (counter-rotating) vortices located near the lower left and right of the domain. As shown, these tend to increase in size with increasing Reynolds number. For  $Re = 3,000$ , an additional secondary vortex develops along the upper left side.

Quantitative comparisons of velocity results between the LBM and N-S method are shown in Figure 8. The results correspond to the three aforementioned Reynolds numbers, and mesh/lattice resolutions of 100x100.

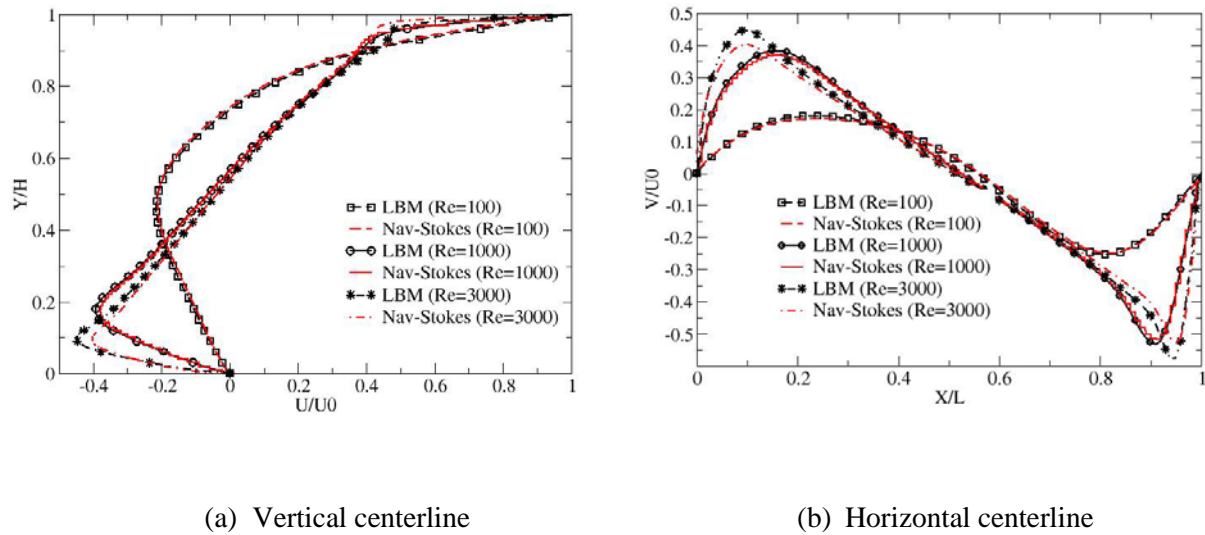
As expected, in the vertical direction (Figure 8(a)), the general x-velocity profiles show maximum positive velocities near  $Y/H=1$ , a direction change at approximately  $Y/H=0.5$ , and maximum negative x-velocities for  $0.1 \leq Y/H \leq 0.2$ . Correspondingly, in the horizontal direction (Figure 8(b)) the y component of velocity shows maximum positive velocities for  $0.1 \leq X/L \leq 0.2$ , a change in direction near  $X/L = 0.5$ , and maximum negative velocities at approximately  $0.89 \leq X/L \leq 0.95$ . Comparisons between the two methods, along the vertical and horizontal centerlines, are in general excellent and reveal minimal differences, particularly for  $Re = 100$ , and  $Re=1,000$ . For  $Re=3,000$  however, some disparity is observed particularly along the upper and lower limits of  $Y/H$ . This is likely the result of the increased compressibility effects associated with larger Reynolds numbers and the limitations of the LBM in handling these cases (as described in Chapter 5).

Figure 7. Velocity contours comparing the results of the LBM and Navier-Stokes for flow through a lid-driven cavity ( $Re = 100$ ,  $Re = 1,000$  and  $Re = 3,000$ ). As shown, the presence of a large central vortex is observed for each case, as well as several secondary vortices (lattice/grid resolution:100x100).



(c) NS;  $Re=1,000$ (d) LBM;  $Re=1,000$ (e) NS;  $Re=3,000$ (f) LBM;  $Re=3,000$

**Figure 8.** Velocity profiles comparing the results of the LBM and NS for flow through a lid-driven cavity ( $Re = 100$ ,  $Re = 1,000$  and  $Re = 3,000$ ). As indicated, the x-component and y-component of velocity were sampled along the vertical and horizontal domain centerlines, respectively.



### 6.3 Rectangular channel flow with back-step

#### 6.3.1 Problem description and setup

A third CFD benchmark problem investigated in this report involves the laminar incompressible flow over a back-step. In contrast to turbulent flows (wherein a single recirculation zone is created just aft of the step), laminar flows exhibit various recirculation zones occurring downstream of the step. Flow separation occurs when adverse pressure gradients act on the fluid. For a low-to-moderate initial Reynolds number, the first region of separation occurs just aft of the step along the bottom wall. With increasing Reynolds number, a second region of separation occurs along the top wall. Further increases in the Reynolds number create yet a third separation region downstream of the first recirculation region along the bottom wall. In fact, recirculation zones will continue to develop downstream in this manner as long as the Reynolds number continues to increase and the flow remains laminar. Of course this is rarely observed, as the flow eventually becomes turbulent (Jongebloed 2008).

The benchmark problem used in this study consists of a channel with a backward-facing step at the entry (Figure 9). As shown, the height of the

back-step is half that of the channel, and extends one channel height ( $H = 0.02$  m) before it opens to the flow. The length of the channel ( $L=25H$ ) is long enough for the flow to become fully developed (as determined from the rectangular channel flow discussion in Section 6.1). The flow is driven by a constant inlet velocity condition with no-slip (zero velocity) conditions at the upper and lower walls.

For this problem, comparisons between the LB and NS methods are conducted for three different Reynolds numbers ( $Re = 200$ ,  $Re = 400$ , and  $Re = 800$ ). An additional simulation is conducted for  $Re = 1,000$  (using solely the LBM) to illustrate the vortex evolution (via contour plots) associated with increasing Reynolds numbers. The corresponding input parameters are equivalent to the rectangular channel flow of Section 6.1, and are shown in Table 3. A constant lattice/grid resolution of 1,000x40 is maintained for each case.

Figure 9. Geometry corresponding to the flow over a back-step.

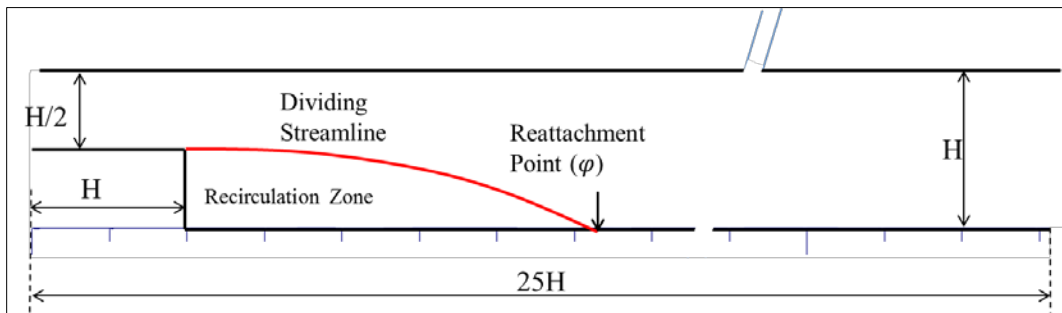
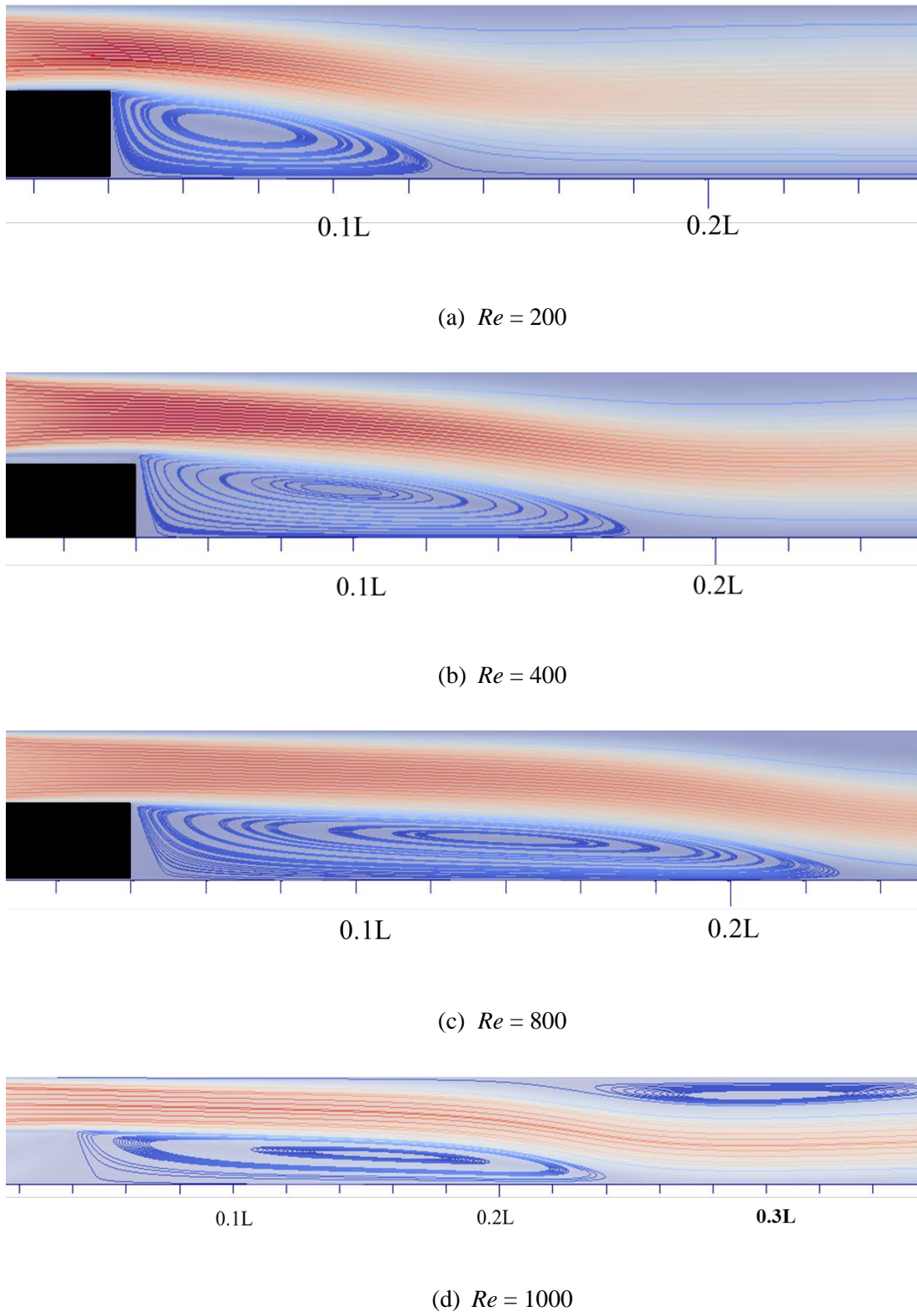


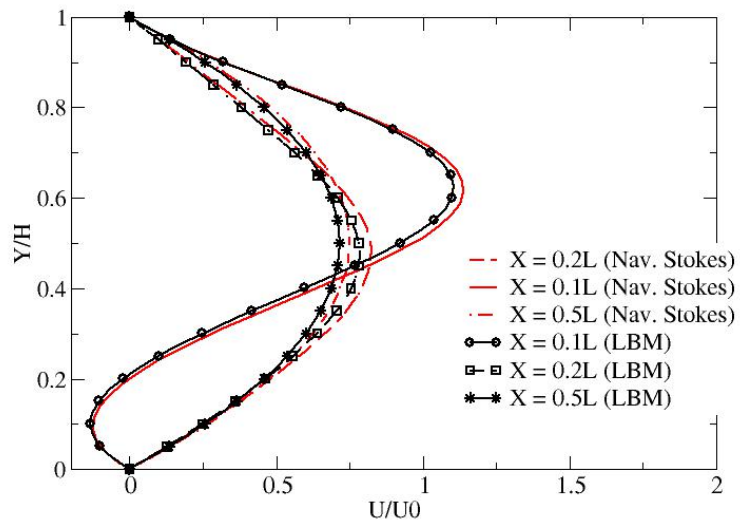
Table 3. Simulation parameters used for the back-step channel flow problem.

Case	Inlet Vel. ( $U_{in}$ ), Nav-Stokes [m/s]	Inlet Vel. ( $U_{lat}$ ) LB [ $\hat{l}/\hat{t}$ ]	Kin. Visc. ( $\nu$ ), Nav-Stokes [m <sup>2</sup> /s]	Kin. Visc. ( $\hat{\nu}$ ), LB [ $\hat{l}^2/\hat{t}$ ]
$Re = 200$	0.01	0.05	1.0E-6	0.01
$Re = 400$	0.02	0.20	1.0E-6	0.02
$Re = 800$	0.04	0.10	1.0E-6	0.005
$Re = 1,000$	—	0.10	—	0.004

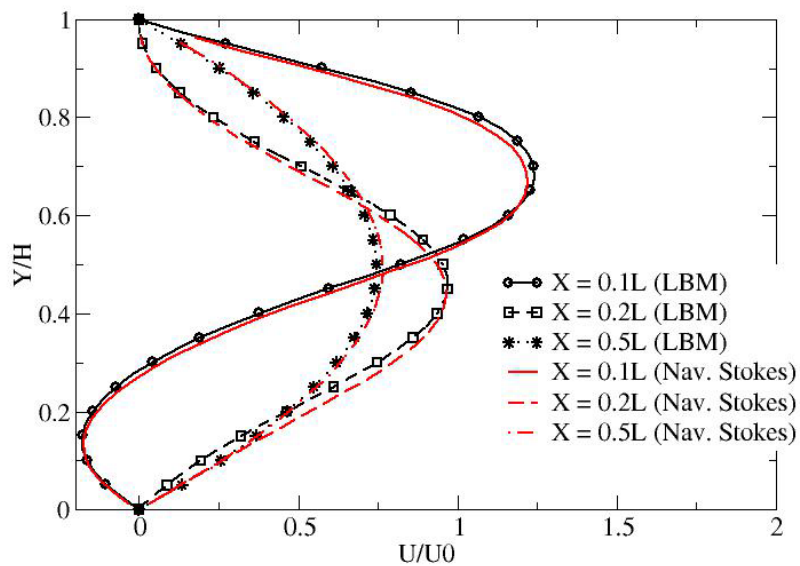
Figure 10. Velocity contours for  $Re = 200$  (a),  $Re = 400$  (b),  $Re = 800$  (c), and  $Re = 1000$  (d) were conducted using the LBM. The contours show a large vortex aft of the back-step (as well as a secondary circulation zone for  $Re = 1,000$ ) that increases in size with increasing Reynolds number (lattice/grid resolution:100x100).



**Figure 11.** Velocity profiles comparing the results of the LBM and NS corresponding to the flow over a back-step ( $Re = 200$  (a),  $Re = 400$  (b) and  $Re = 800$  (c)). As indicated, the velocities were sampled at three downstream locations corresponding to  $X/L = 0.1$ ,  $X/L = 0.2$  and  $X/L = 0.5$  (lattice/grid resolution = 1,000x40).



(a)  $Re = 200$



(b)  $Re = 400$

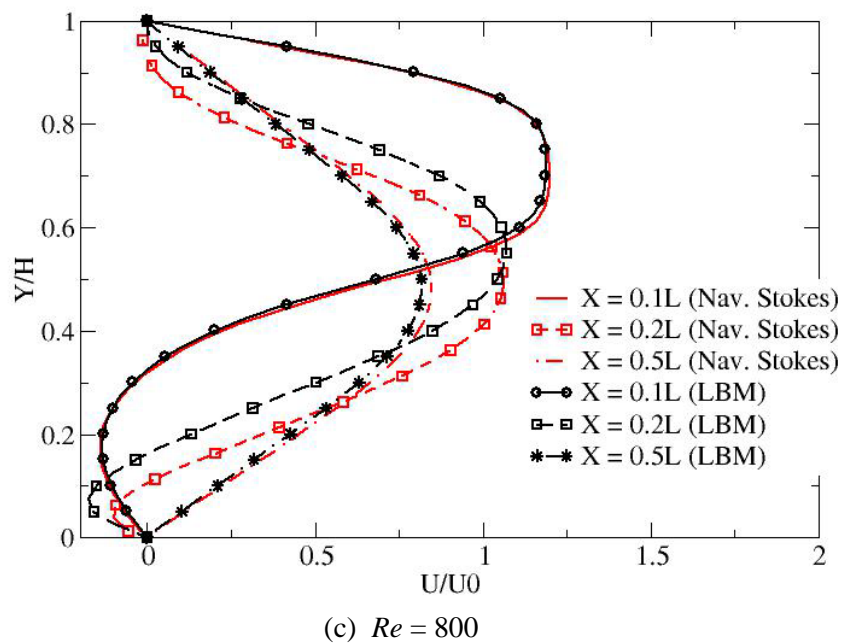
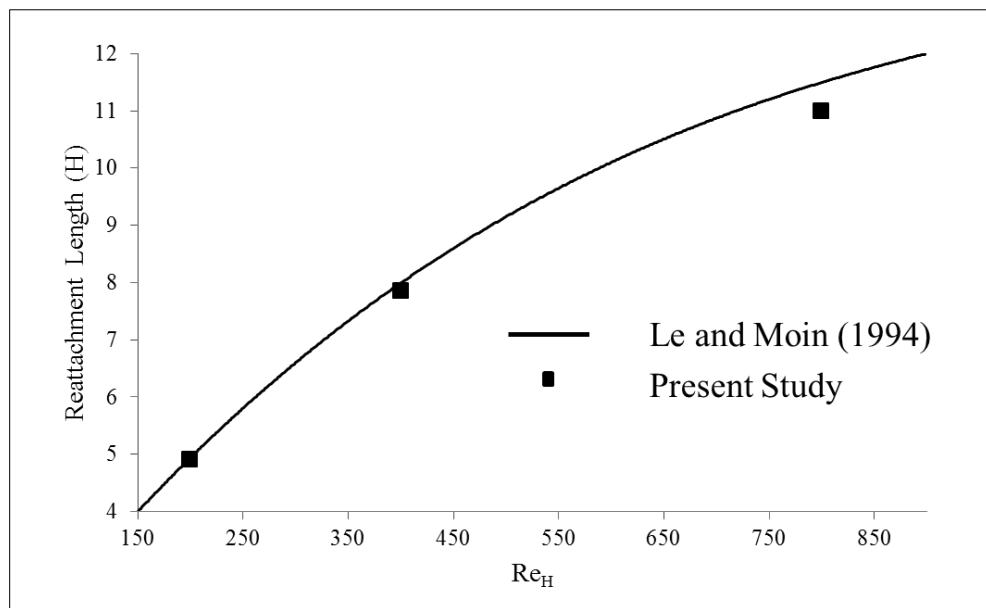
(c)  $Re = 800$ 

Figure 12. Reattachment distance as a function of Reynolds number. Results using the LBM are compared with the experiments conducted by Le and Moin (1994).



### 6.3.2 Results

The velocity contours conducted with the LBM are shown in Figure 10 and correspond to  $Re = 200$ ,  $Re = 400$ ,  $Re = 800$  and  $Re = 1,000$ . As shown, the presence of an initial recirculation zone just aft of the back-step is evident for each case. A shear layer divides this zone from the upper streamlines as shown. The recirculation zone tends to increase in size (along the X-direction) with increasing Reynolds number. Also shown, for  $Re = 1000$ , is the presence of a secondary vortex forming on the upper wall with center at approximately  $X = 0.3L$ . As previously stated, this accumulation of downstream vortices is a characteristic of all laminar incompressible back-step flows as long as the Reynolds number continues to increase.

The velocity profiles comparing the results of the LBM and Navier-Stokes method are shown in Figure 11. The results correspond to  $Re = 200$ ,  $Re = 400$  and  $Re = 800$ . As shown, the velocity distribution along the downstream direction progressively evolves into a characteristic parabolic profile as the flow becomes fully developed. In the upstream region (for  $X = 0.1L$ ), the presence of the back-step is evident as the velocity profile becomes asymmetric particularly for  $Y/H < 0.3$ .

Comparisons between the LBM and NS method are good, particularly at lower Reynolds numbers ( $Re = 200$ , and  $Re = 400$ ). At  $Re = 800$ , some disparity between the methods is observed at  $X/L = 0.2L$ , corresponding to the circulation region just short of the reattachment point, as seen in Figure 11(c).

Additional comparisons with the experimental work of Le et al. (1997) were made with respect to the reattachment point. As illustrated in Figure 9, this point is defined as the  $X$  location, where the dividing streamline (located between the shear layer and the recirculation zone) reattaches to the lower channel wall. As shown in Figure 12, the present work agrees well with that of Le et al. (1997). We note that Le et al. used a Reynolds number based on the maximum velocity (e.g.,  $u_{max} = 3\bar{u}/2$ ), and the appropriate adjustments were made here.

## 6.4 Flow over a stationary circular cylinder

### 6.4.1 Problem description and setup

The final benchmark problem involves the laminar incompressible flow over a stationary circular cylinder. This particular flow is one of the most widely studied in the CFD literature, and is well known for its ability to illustrate the transition from steady to unsteady flow behavior as a function of Reynolds number. As shown in Figure 13, at very low Reynolds number ( $Re \ll 1$ ) the flow is steady with no boundary layer separation. As  $Re$  approaches 10, the flow remains steady, but boundary layer separation begins and evolves to form two symmetric vortices in the wake region. For Reynolds numbers in excess of 90 (but less than  $\sim 10^4$ ), although it remains laminar, the flow becomes unsteady and asymmetric. Von Karman vortex shedding is observed and distinguished by regular shear layer separation from the upper and lower surfaces of the cylinder. Beyond  $Re = \sim 10^4$  the flow becomes turbulent.

The geometry for this problem is shown in Figure 14. As shown, a cylinder of radius  $R$  ( $R=0.1m$ ) is placed  $6.6R$  from the inlet and  $3R$  from the top and bottom of a channel of length  $40R$ . For boundary conditions, a uniform inlet velocity is imposed at the inlet, and a standard outflow boundary at the exit. The upper and lower channel walls are designated as no-slip (zero velocity) conditions (implemented with standard bounce-back conditions for the LBM simulation).

While most LBM simulations commonly apply the standard bounce-back conditions to the wall of the circular cylinder, this action results (for a regular hexagonal lattice) in an irregular “stair-step” geometry. The effect on the flow field response is clearly non-ideal, as this irregular surface would (like the effect of dimples on a golf ball) delay boundary layer separation and result in atypical results. For this reason, the IMB method is invoked (Owen et al. 2011; as discussed in Chapter 6). In particular, the quantity ( $\varepsilon$ ) that represents the area fraction (volume fraction in 3D) of the circular cylinder with an intersecting lattice cell is computed and then used to modify the collision operator.

**Figure 13.** Illustration of velocity profiles as a function of Reynolds number ([http://en.wikipedia.org/wiki/Reynolds\\_number](http://en.wikipedia.org/wiki/Reynolds_number)).

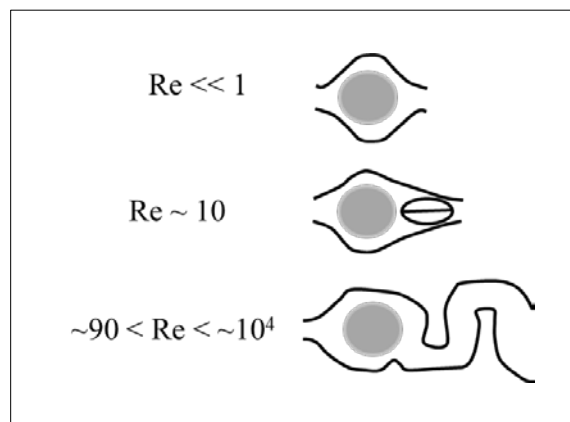
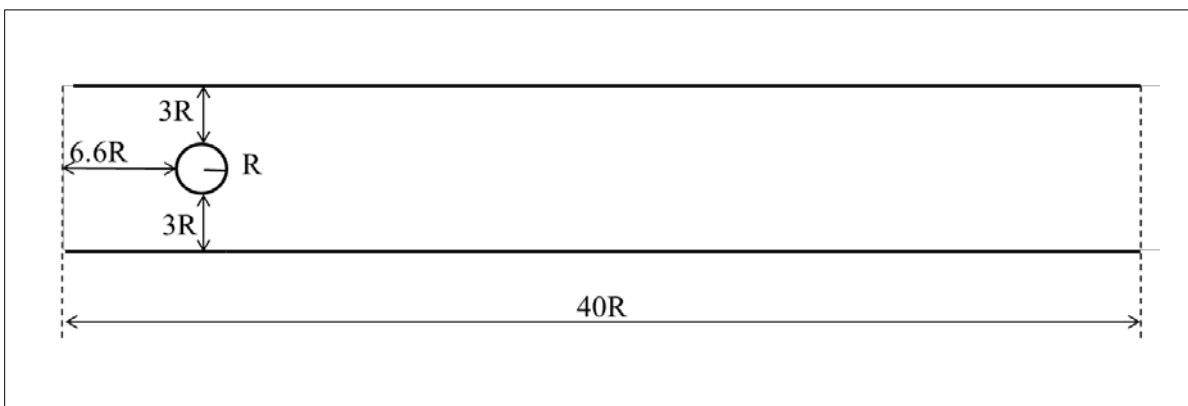


**Figure 14.** Geometry corresponding to the flow over a stationary circular cylinder.



For this work, three different Reynolds numbers were investigated:  $Re_D=1$ ,  $Re_D=10$ , and  $Re_D=120$ , where  $D$  corresponds to the cylinder diameter. The corresponding input parameters for both the NS method and LBM are shown in Table 4. A constant lattice/grid resolution of 2000x400 is maintained throughout.

Lastly, for comparison purposes with our experiment, the Coefficient of Drag ( $C_d$ )<sup>\*</sup> is computed in Eq. 66:

---

\* "Coefficient of Drag," <http://www.aerospaceweb.org/question/aerodynamics/q0231.shtml>, accessed 24 April 2014.

$$C_D = \frac{F_x}{1/2\rho U^2 A} \quad (66)$$

where  $F_x$  is the x component of the total fluid force acting on the cylinder, and  $A$  is the projected area. For the LBM, the total force ( $\vec{F}$ ) over the cylinder is computed via the momentum exchange method, as shown in Eq. 67 (Owen et al. 2011):

$$\vec{F} = \frac{\delta_x^3}{\delta_t} \sum_n B_n (\sum_i \Omega_i^s \vec{e}_i) \quad (67)$$

where  $B_n$ ,  $\Omega_i^s$ ,  $\delta_t$ ,  $\vec{e}_i$ , and  $\delta_x$  have been previously defined in Chapter 6.

**Table 4. Simulation parameters used for the back-step channel flow problem.**

Case	Inlet Vel. ( $U_{in}$ ), Nav-Stokes [m/s]	Inlet Vel. ( $U_{lat}$ ) LB [ $\hat{l}/\hat{t}$ ]	Kin. Visc. ( $\nu$ ), Nav-Stokes [m <sup>2</sup> /s]	Kin. Visc. ( $\hat{\nu}$ ), LB [ $\hat{l}^2/\hat{t}$ ]
Re=1	0.000005	0.00167	1.0E-6	0.167
Re=10	0.00005	0.0167	1.0E-6	0.167
Re=120	0.0006	0.2	1.0E-6	0.167

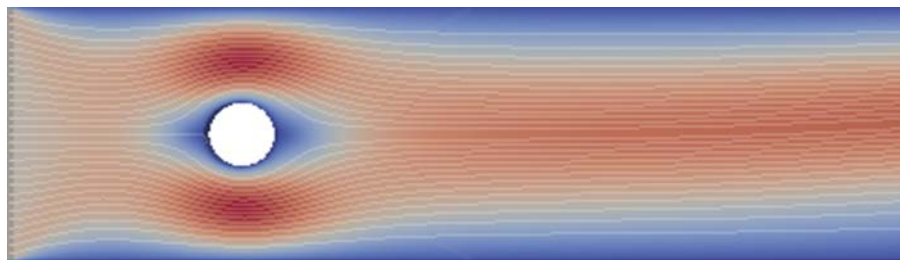
#### 6.4.2 Results

The velocity contours of both the LBM and NS method are shown in Figure 15 and correspond to  $Re = 1$ ,  $Re = 10$ , and  $Re = 120$ . As shown, both sets of simulation results are qualitatively equivalent, reflecting the changes in velocity contours with respect to Reynolds number in accordance with the expected profiles shown in Figure 13.

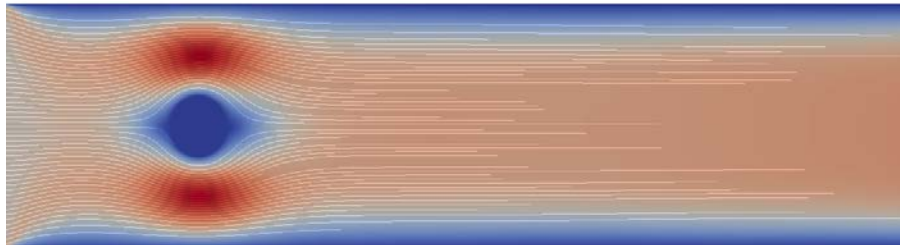
Quantitative comparisons of velocity between the LBM and NS method are shown in Figure 16 and correspond to  $Re = 1$  and  $Re = 10$ . As indicated, in both cases the velocity distribution at the downstream location ( $X/L = 0.5$ ) progressively evolves into a characteristic parabolic profile as the flow becomes fully developed. At an upstream location forward of the cylinder ( $X/L = 0.1$ ), the presence of the stationary cylinder is clearly observed as the velocity profiles along  $Y/L = 0.5$  gradually decrease towards the point of stagnation. The presence of the expanding wake region for  $Re=10$  is also evident at  $X/L = 0.2$ , as indicated by the significant decrease in velocity at  $Y/H = 0.5$ .

For the case of  $Re=120$ , the average drag coefficient  $\langle C_d \rangle$  was computed in accordance with Eq. 66 and 67. As shown in Figure 17, a constant shedding frequency was observed after approximately 25,000 iterations ( $U_{ot}/D = 12.5$ ). The computed drag coefficient of 0.97 compared favorably with the experimental results ( $\sim 0.98 - \sim 0.99$ ) found in the experimental literature (Aerospace.org).

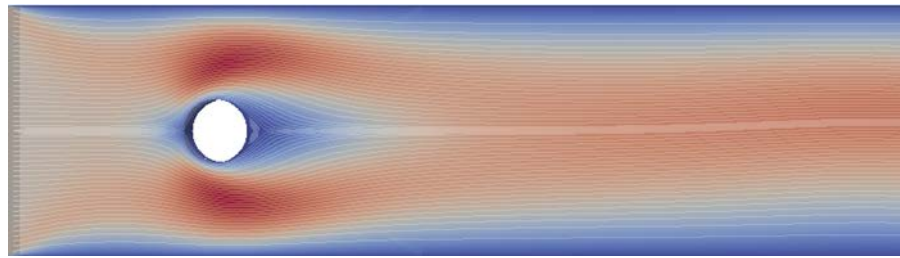
Figure 15. Velocity contours for  $Re = 1$ ,  $Re = 10$ , and  $Re = 120$  show results from both the LBM and NS method. The contours reveal the characteristic steady to unsteady flow behaviors associated with increasing Reynolds number, and show the presence of Von Karman vortex shedding for  $Re = 120$ . (Lattice/grid resolution: 2000x400.)



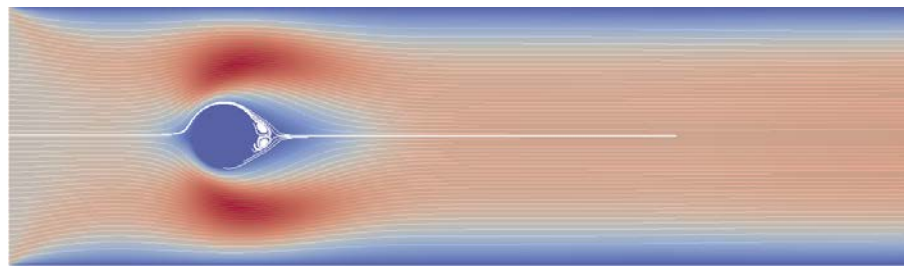
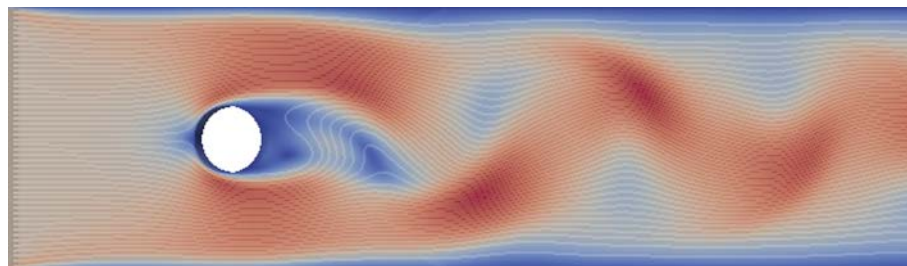
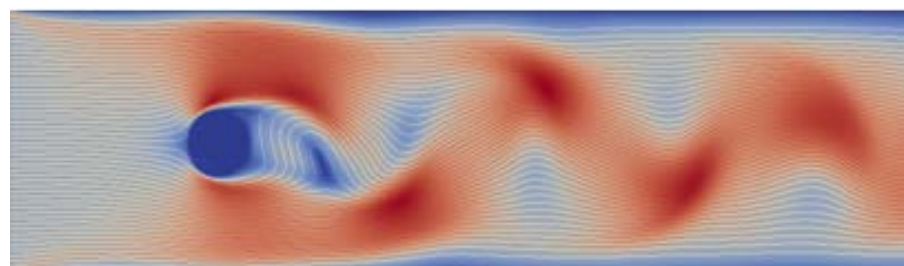
NS;  $Re = 1$



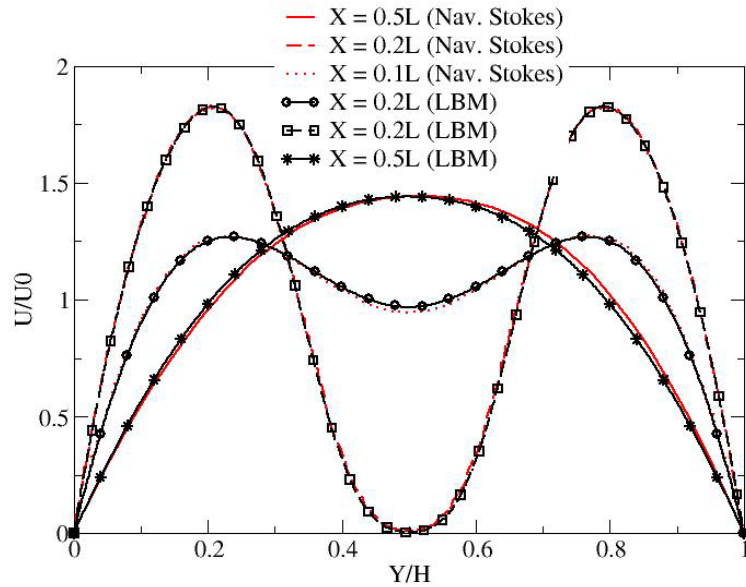
LBM;  $Re = 1$



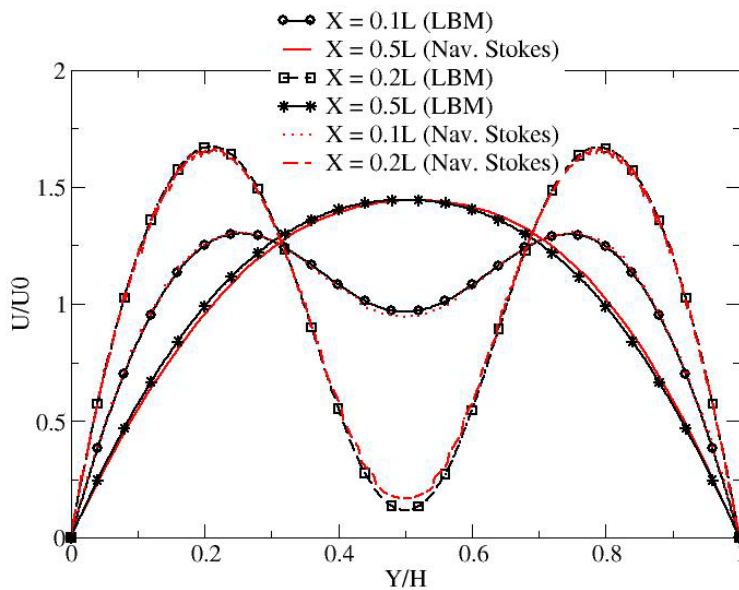
NS;  $Re = 10$

LBM:  $Re = 10$ (d) NS;  $Re = 120$ (e) LB;  $Re = 120$

**Figure 16.** Velocity profiles comparing the results of the LB and NS methods corresponding to the flow over a stationary circular cylinder ( $Re = 1$ , and  $Re = 10$ ). As indicated, the velocities were sampled at three downstream locations corresponding to  $X/L = 0.1$ ,  $X/L = 0.2$  and  $X/L = 0.5$ . (Note: lattice/grid resolution = 2,000x400).

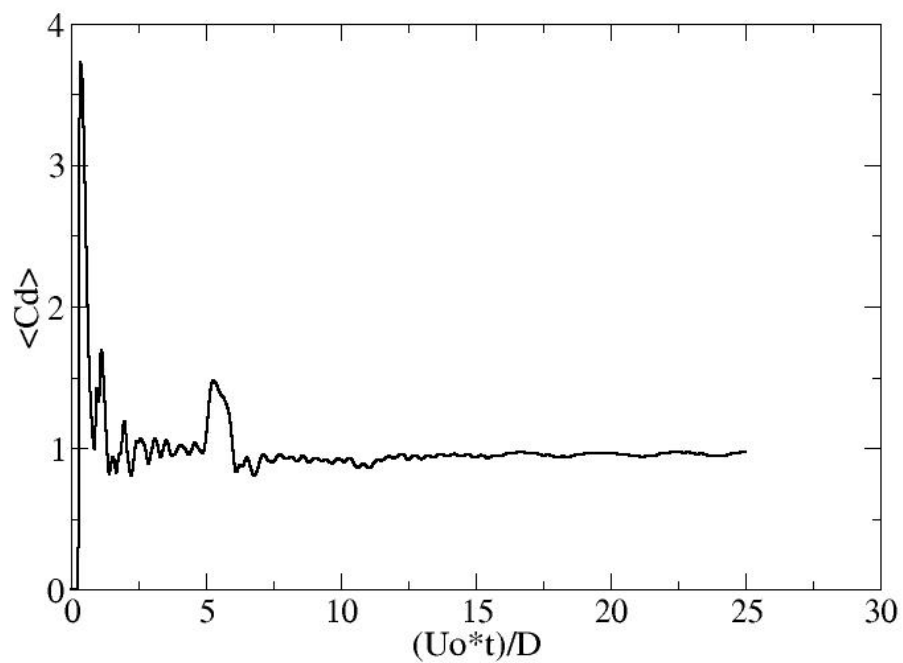


(a)  $Re = 10$



(b)  $Re = 1$

Figure 17. Time history of the drag coefficient computed using Eq. 66. The results shown are from the LBM for  $Re=120$ .



## 7 Summary and Conclusions

This report documented a comparison/validation effort accompanying the development of a standard Lattice Boltzmann solver which is to be coupled to an existing ERDC Discrete Element Model. The primary goal was to validate the Lattice Boltzmann model by comparing it with various laminar, incompressible flow cases simulated using a finite volume-based Navier-Stokes solver. Simulations involving four standard benchmark studies were analyzed: (1) the flow through a rectangular channel, (2) the flow through a lid-driven cavity, (3) the flow over a back-step, and (4) the flow over a stationary circular cylinder. For these specific applications and the Reynolds numbers simulated, the results showed excellent agreement between the two cases. Limitations in the LBM at some elevated Reynolds numbers were due primarily to compressibility effects. However, even these cases showed only marginal deviation from the finite volume Navier-Stokes method.

## References

- Aerospaceweb.org. 2012. "Drage of Cylinders and Cones." Accessed online 24 April 2014: <http://www.aerospaceweb.org/question/aerodynamics/q0231.shtml>.
- Alexander, F. J., H. Chen, S. Chen, and G. D. Doolen. 1992. "Lattice Boltzmann Model for Compressible Fluids." *Physical Review A: Atomic, Molecular, and Optical Physics*. 46(4):1967.
- Al-Jahmany, Yarub Y. 2004. "Comparative Study of Lattice-Boltzmann and Finite Volume Methods for the Simulation of Non-Newtonian Fluid Flows through a Planar Contraction." *International Journal for Numerical Methods in Fluids* 46(9): 903-920.
- Allen, Jeffrey B. 2006. "Direct Simulation Monte Carlo Simulations of Aerodynamic Effects on Sounding Rockets." PhD Dissertation, Utah State University.
- Canuto, Claudio, M. Yousuff Hussaini, Alfio Quarteroni, and Thomas A. Zang. 1988. *Spectral Methods in Fluid Dynamics* (from Springer series in computational physics). Berlin: Springer-Verlag.
- Chapman, Sydney, and T.G. Cowling. 1991. *The Mathematical Theory of Non-Uniform Gases: An Account of the Kinetic Theory of Viscosity, Thermal Conduction and the Diffusion in Gases*. Third edition. New York: The Cambridge University Press.
- Chen, Shiyi, Hudong Chen, Daniel Martnez, and Wwilliam Matthaeus. 1991. "Lattice Boltzmann Model for Simulation of Magnetohydrodynamics." *Physical Review Letters*. 67(27): 3776–3779.
- d'Humières, Dominique. 1994. "Generalized lattice Boltzmann Equations." In *Rarefied Gas Dynamics: Theory and Simulations*, edited by B.D. Shizgal and D.P. Weaver, 450–458. Reston, VA: American Institute of Aeronautics and Astronautics. doi: [10.2514/5.9781600866319.0450.0458](https://doi.org/10.2514/5.9781600866319.0450.0458).
- d'Humières, Dominique, Irina Ginzburg, Manfred Krafczyk, Pierre Lallemand, and Li-Shi Luo. 2002. "Multiple-Relaxation-Time Lattice Boltzmann Models in Three Dimensions." *Philosophical Transactions of the Royal Society of London, Series A* 360(1792): 437–451. doi: [10.1098/rsta.2001.0955](https://doi.org/10.1098/rsta.2001.0955).
- Eggels, Jack G.M. 1996. "Direct and Large-Eddy Simulation of Turbulent Fluid Flow Using the Lattice- Boltzmann Scheme." *International Journal of Heat and Fluid Flow* 17(3): 307–323. doi: [10.1016/0142-727X\(96\)00044-6](https://doi.org/10.1016/0142-727X(96)00044-6).
- Frisch, Uriel D. Dominique d'Humières, Brosl Hasslacher, Pierre Lallemand, Yves Pomeau, and Jean-Pierre Rivet. 1987. "Lattice Gas Hydrodynamics in Two and Three Dimensions." *Complex Systems* 1(4):649–707.
- Griebel, Michael, Thomas Dornseifer, and Tilman Neunhoefer. 1997. *Numerical Simulation in Fluid Dynamics: A Practical Introduction*. Book 3 in series, Monographs on Mathematical Modeling and Computations. Philadelphia: Society for Industrial and Applied Mathematics.

- Grunau, Daryl, Shiyi Chen, and Kenneth Eggert. 1993. "A Lattice Boltzmann Model for Multi-phase Fluid Flows." *Physics of Fluids A* 5: 2557 doi: [10.1063/1.858769](https://doi.org/10.1063/1.858769)
- Gunstensen, Andrew K., Daniel H. Rothman, Stephanie Zaleski, and Gianluigi Zanetti. 1991. "Lattice Boltzmann Model of Immiscible Fluids." *Physical Review A* 43(8)4320–4327.
- Han, Yanhui, and Peter A. Cundall. 2013. "LBM-DEM Modeling of Fluid-Solid Interaction in Porous Media." *International Journal for Numerical and Analytical Methods in Geomechanics* 37(10): 1391-1407. doi: [10.1002/nag.2096](https://doi.org/10.1002/nag.2096).
- Henderson, Amy. 2007. *The ParaView Guide: A Parallel Visualization Application*. New York: Kitware Inc.
- Higuera, F. J., and J. Jimenez. 1989. "Boltzmann Approach to Lattice Gas Simulations." *Europhysics Letters* 9(7):663–668.
- Issa, Raad I. 1986. "Solution of the Implicitly Discretized Fluid Flow Equations by Operator Splitting." *Journal of Computational Physics* 62(1): 40-65. doi: [10.1016/0021-9991\(86\)90099-9](https://doi.org/10.1016/0021-9991(86)90099-9).
- Jongebloed, Luke. 2008. "Numerical Study using FLUENT of the Separation and Reattachment Points for Backwards-Facing Step Flow." Masters Thesis. Hartford, CT: Rensselaer Polytechnic Institute.  
[http://www.ewp.rpi.edu/hartford/users/papers/engr/ernesto/xie4/ME\\_Project/Important%20Files/Reference/Masters%20Project%20-%20LU%20--FINAL\\_2.pdf](http://www.ewp.rpi.edu/hartford/users/papers/engr/ernesto/xie4/ME_Project/Important%20Files/Reference/Masters%20Project%20-%20LU%20--FINAL_2.pdf)
- Koelman, J.M.V.A. 1991. "A Simple Lattice Boltzmann Scheme for Navier-Stokes Fluid Flow." *Europhysics Letters* 15 (6):603–607.
- Ladd, A.J.C., and R. Verberg. 2001. "Lattice-Boltzmann Simulations of Particle-Fluid Suspensions." *Journal of Statistical Physics* 104(5–6): 1191–1251.
- Le, Hung, Parviz Moin, and John Kim. 1997. "Direct Numerical Simulation of Turbulent Flow over a Backward-Facing Step." *Journal of Fluid Mechanics* Vol. 330: 349–374.
- Maier, Robert S., Robert S. Bernard, and Daryl W. Grunau, 1996. "Boundary Conditions for the Lattice Boltzmann Method." *Physics of Fluids* 8: 1788.  
<http://dx.doi.org/10.1063/1.868961>
- Maier, Robert S., and Robert S. Bernard. 1997. "Accuracy of the Lattice Boltzmann Method," *International Journal of Modern Physics C* 8(4): 747.
- Maier, Robert S., D. M. Kroll, Y.E. Kutsovsky, H.T. Davis, and Robert S. Bernard. 1998. "Simulation of Flow through Bead Packs Using the Lattice Boltzmann Method." *Physics of Fluids* 10(1): 60–74. <http://dx.doi.org/10.1063/1.869550>
- Mohamad, A.A. 2011. *Lattice Boltzmann Method: Fundamentals and Engineering Applications with Computer Codes*. London: Springer-Verlag.

- Owen, D.R.J., C.R. Leonardi, and Y.T. Feng. 2011. "An Efficient Framework for Fluid-Structure Interaction Using the Lattice Boltzmann Method and Immersed Moving Boundaries." *International Journal for Numerical Methods in Engineering* 87(1-5):66-95. doi: 10.1002/nme.2985.
- Qian, Y. H., D. d'Humieres, and P. Lallemand. 1992, "Lattice BGK Models for Navier-Stokes Equation." *Europhysics Letters* 17(6): 479–484. doi:10.1209/0295-5075/17/6/001.
- Raabe, D. 2004. "Overview of the Lattice Boltzmann method for Nano- and Microscale Fluid Dynamics in Material Science and Engineering," *Modelling and Simulation in Materials Science and Engineering* 12(6):R13.
- Shan, Xiaowen, and Hudong Chen. 1993. "Lattice Boltzmann Model for Simulating Flows with Multiple Phases and Components." *Physical Review E: Statistical Physics, Plasmas, Fluids, and Related Interdisciplinary Topics* 47: 1815–1819.
- Succi, Sauro, Olga Filippova, Greg Smith, and Efthimios Kaxiras. 2001. "Applying the Lattice Boltzmann Equation to Multiscale Fluid Problems." *Computing in Science and Engineering* 3(6): 26–37.
- Sun, WaiChing, Matthew R. Kuhn, and John W. Rudnicki. 2013. "A Multiscale DEM-LBM Analysis on Permeability Evolutions Inside a Dilatant Shear Band." *Acta Geotechnica* 8(5):465–480.
- Third, J.R., and C. R. Müller. 2013. "Coupled LBM-DEM Simulations of Gas Fluidised Beds." In *The 14th International Conference on Fluidization – From Fundamentals to Products*. Accessed online Engineering Conferences International (ECI) Digital Archives: [http://dc.engconfintl.org/fluidization\\_xiv/97](http://dc.engconfintl.org/fluidization_xiv/97).
- Varnik, F., A. Rios, M. Gross, and I. Steinbach. 2013. "Simulation of Viscous Sintering using the Lattice Boltzmann Method." *Modelling and Simulation in Materials Science and Engineering* 21(2).
- Versteeg, Henk Kaarle, and Weeratunge Malalasekera. 1995. *An Introduction to Computational Fluid Dynamics: The Finite Volume Method*. Pearson Prentice Hall.
- Viggen, Erland M. 2009. "The Lattice Boltzmann Method with Applications in Acoustics." Thesis. Trondheim, Norway: NTNU Dept. of Physics.
- Zienkiewicz, O. C., R. L. Taylor, and P. Nithiarasu. 2005. *The Finite Element Method for Fluid Dynamics*, Sixth Edition. Oxford: Butterworth-Heinemann.
- Zou, Qisu, Shuling Hou, Shiyi Chen, and Gary D. Doolen. 1995. "An Improved Incompressible Lattice Boltzmann Model for Time-Independent Flows." *Journal of Statistical Physics* 81(1-2):35–48.
- Zou, Qisu, and Xiaoyi He. 1997. "On Pressure and Velocity Boundary Conditions for the Lattice Boltzmann BGK Model." *Physics of Fluids* 9(6): 1591-1598.

---

(This page intentionally left blank.)

## Appendix A: Derivation of the Equilibrium Distribution Function

The equilibrium distribution function can be derived from the Maxwell-Boltzmann velocity distribution. As a function of energy ( $E$ ), this can be written as Eq. A1:

$$f(E) = A \exp\left(-\frac{E}{k_B T}\right) \quad (\text{A1})$$

Where  $k_B$  is the Boltzmann constant,  $A$  is a constant, and  $T$  is the temperature.

For a free gas (particle energy is solely kinetic), we can write the function in terms of the velocity of a particle as Eq. A2:

$$f(\vec{v}) = A \exp\left(-\frac{0.5m\vec{v}^2}{k_B T}\right) \quad (\text{A2})$$

Using the normalization condition (i.e.,  $\int f(\vec{v}) d^3v = 1$ ), we obtain the value for  $A$ , and  $f(\vec{v})$  becomes Eq. A3:

$$f(\vec{v}) = \left(\frac{m}{2\pi k_B T}\right)^{1/2} \exp\left[-\frac{m\vec{v}^2}{2k_B T}\right] \quad (\text{A3})$$

Rewriting the velocity in terms of its mean ( $\vec{u}$ ) and deviation ( $\vec{c}_i$ ) as:  $\vec{v} = \vec{c}_i - \vec{u}$ , and using the isothermal ideal gas relation:  $c_s^2 = k_B T/m$ , we have Eq. A4:

$$f \propto \exp\left[-\frac{(\vec{c}_i - \vec{u})^2}{2c_s^2}\right] \propto \exp\left[-\frac{\vec{c}_i^2}{2c_s^2}\right] \exp\left[-\frac{u^2 - 2u \cdot c_i}{2c_s^2}\right] \quad (\text{A4})$$

Using the Taylor series expansion ( $e^x = 1 + x + \frac{x^2}{2!} + \dots$ ) and dropping terms of order three and above, gives Eq. A5:

$$\exp\left[-\frac{u^2 - 2u \cdot c_i}{2c_s^2}\right] \approx 1 + \frac{u \cdot c_i}{c_s^2} + \frac{(u \cdot c_i)^2}{2c_s^4} - \frac{u^2}{2c_s^2} + \mathcal{O}(u^3) \quad (\text{A5})$$

Since along with the collision operator ( $\Omega$ ) the equilibrium function must preserve both mass and momentum, as shown in Eq. A6 and Eq. A7:

$$\rho = \sum_i f_i^{(0)} = \sum_i f_i \quad (\text{A6})$$

$$\rho \vec{u} = \sum_i \vec{c}_i f_i^{(0)} = \sum_i \vec{c}_i f_i \quad (\text{A7})$$

It can be shown that the constant of proportionality ( $K$ ) is simply  $\rho$  (Viggen 2009). This gives us the final generalize form of the equilibrium function as Eq. A8:

$$f_i^{(0)} = \rho t_i \left[ 1 + \frac{u \cdot c_i}{c_s^2} + \frac{(u \cdot c_i)^2}{2c_s^4} - \frac{u^2}{2c_s^2} \right] \quad (\text{A8})$$

# REPORT DOCUMENTATION PAGE

*Form Approved  
OMB No. 0704-0188*

Public reporting burden for this collection of information is estimated to average 1 hour per response, including the time for reviewing instructions, searching existing data sources, gathering and maintaining the data needed, and completing and reviewing this collection of information. Send comments regarding this burden estimate or any other aspect of this collection of information, including suggestions for reducing this burden to Department of Defense, Washington Headquarters Services, Directorate for Information Operations and Reports (0704-0188), 1215 Jefferson Davis Highway, Suite 1204, Arlington, VA 22202-4302. Respondents should be aware that notwithstanding any other provision of law, no person shall be subject to any penalty for failing to comply with a collection of information if it does not display a currently valid OMB control number. PLEASE DO NOT RETURN YOUR FORM TO THE ABOVE ADDRESS.

<b>1. REPORT DATE (DD-MM-YYYY)</b> 15-Sep-2014			<b>2. REPORT TYPE</b> Final		<b>3. DATES COVERED (From - To)</b>	
<b>4. TITLE AND SUBTITLE</b>  Comparison/Validation Study of Lattice Boltzmann and Navier Stokes for Various Benchmark Applications: Report 1 in "Discrete Nano-Scale Mechanics and Simulations" Series			<b>5a. CONTRACT NUMBER</b>			
			<b>5b. GRANT NUMBER</b>			
			<b>5c. PROGRAM ELEMENT NUMBER</b> AT22/AT40			
<b>6. AUTHOR(S)</b>  Jeffrey B. Allen, Wayne D. Hodo, Laura Walizer, David P. McInnis, Alex Carrillo, Bohumir Jelinek, Daniel Johnson, John Peters, and Sergio D. Felicelli			<b>5d. PROJECT NUMBER</b>			
			<b>5e. TASK NUMBER</b>			
			<b>5f. WORK UNIT NUMBER</b> PM001 and MR001			
<b>7. PERFORMING ORGANIZATION NAME(S) AND ADDRESS(ES)</b>  US Army Engineer Research and Development Center 3909 Halls Ferry Road Vicksburg, MS 39180-6199			<b>8. PERFORMING ORGANIZATION REPORT NUMBER</b> ERDC TR-14-6			
<b>9. SPONSORING / MONITORING AGENCY NAME(S) AND ADDRESS(ES)</b>  Headquarters US Army Corps of Engineers 441 G Street NW Washington DC 20314-1000			<b>10. SPONSOR/MONITOR'S ACRONYM(S)</b> USACE			
			<b>11. SPONSOR/MONITOR'S REPORT NUMBER(S)</b>			
<b>12. DISTRIBUTION / AVAILABILITY STATEMENT</b> Approved for public release; distribution is unlimited.						
<b>13. SUPPLEMENTARY NOTES</b>						
<b>14. ABSTRACT</b>  For purposes relating to the U.S. Army's need for materials modeling and force protection, this work provides justification for assigning effective equivalence between two commonly used fluid simulation methods—namely the Navier-Stokes (NS) and Lattice Boltzmann methods. The Lattice Boltzmann Method (LBM) has become increasingly popular as an alternative approach to traditional NS-based techniques for modeling various incompressible fluid flow applications. The LBM has recently increased its range of applicability to include numerous fields of interest including those involving multiphase and thermo-fluid structure interactions. This report documents a comparison/validation effort accompanying the development of a standard Lattice Boltzmann solver with immersible moving boundaries. The primary goal is to validate the model by comparing it with various laminar, incompressible flow cases simulated using a finite volume-based NS solver. Simulations involving four standard benchmark studies were analyzed: (1) the flow through a rectangular channel, (2) the flow through a lid-driven cavity, (3) the flow over a back-step, and (4) the flow over a stationary circular cylinder. For the specific applications and Reynolds numbers simulated, the results showed excellent agreement between the two cases. Disparities were observed only when the theoretical constraints of the LBM were exceeded.						
<b>15. SUBJECT TERMS</b> Lattice-Boltzmann Method (LBM), Navier-Stokes, modeling, incompressible fluid flow, immersible moving boundary (IMB), channel flow, Reynolds number						
<b>16. SECURITY CLASSIFICATION OF:</b>			<b>17. LIMITATION OF ABSTRACT</b> UU	<b>18. NUMBER OF PAGES</b> 63	<b>19a. NAME OF RESPONSIBLE PERSON</b>	
a. REPORT Unclassified	b. ABSTRACT Unclassified	c. THIS PAGE Unclassified			<b>19b. TELEPHONE NUMBER (include area code)</b>	